submitted to *Geophys. J. Int.*

Joint Inversion of Seismic and Geoelectrical Data Targeting Geological Faults

Mauricio Arboleda-Zapata[1], Olaf A. Cirpka[1], Peter Dietrich[1,2], Emmanuel Léger[3], and Carsten Leven[1]

[1]Department of Geosciences, University of Tübingen, Tübingen, Germany
[2]Department of Monitoring and Exploration Technologies, Helmholtz Centre for Environmental Research (UFZ), Leipzig, Germany
[3]Université Paris-Saclay, CNRS, GEOPS, Orsay, France

SUMMARY

Near-surface geological faults play a crucial role in subsurface systems because they influence fluid flow and transport and can cause geotechnical failure. Topography can sometimes indicate the presence of fault zones, particularly in active tectonic settings where geomorphic features such as triangular facets are preserved. However, particularly for older inactive faults, characteristic surface geomorphic signatures may have completely been removed by erosion, or the fault may be buried beneath younger sediments. Although direct observations from outcrops or borehole data can confirm the presence of a fault very reliably, such data is commonly too sparse and/or distant to precisely constrain fault location in the target area. In this context, near-surface geophysical methods, such as electrical resistivity tomography (ERT) and seismic refraction tomography (SRT), may be useful to locate faults. However, these geophysical data are typically inverted using smoothness-constrained approaches, which can obscure sharp structural features unless the latter are explicitly accounted for in the models. In this study, we present a workflow that enhances the identification of fault zones by jointly inverting collocated ERT and SRT data, considering a parameterization approach based on a layered subsurface model explicitly including a fault. Unlike conventional approaches, we run multiple inversions in which the starting models are initialized with randomly generated fault geometries, guiding the search toward different structural scenarios that yield comparable data misfits. In the absence of additional prior information, these solutions should be interpreted as equally plausible representations of the subsurface. The resulting ensemble of models provides a practical indication of where the structure is well constrained (i.e. features that appear consistently across solutions) and where ambiguity remains (i.e. features that vary among solutions). We showcase the applicability of our workflow with synthetic and field data, where collocated ERT and SRT measurements were collected across expected fault zones. Our results show that the joint inversion of ERT and SRT data consistently narrows the fault location to within a few meters. Iterative incorporation of prior information (e.g., one vs. two boreholes) leads to significant improvements in model geometry and physical property estimates. However, consistent with the intrinsic ambiguity of geophysical inversion, the results remain non-unique; even models depicting opposite fault types (normal vs. reverse) may reproduce the data to comparable levels. This outcome highlights the strength of the workflow in identifying competing structural scenarios that are equally consistent with the observations. Thus, the resulting ensemble provides essential guidance for targeted ground-truthing and follow-up investigations aimed at resolving the remaining ambiguity.

1 INTRODUCTION

Geological faults are key structures in subsurface fluid-flow systems because they can act either as conduits or barriers to fluid migration, depending on their internal architecture and stress regime (e.g., Bense & Person 2006; Tillner et al. 2013). In groundwater systems, faults may connect or isolate aquifers and influence recharge pathways (e.g., Moreira et al. 2025). They must therefore be incorporated into groundwater flow-and-transport models to improve their accuracy and reliability (e.g., Ball et al. 2010; Bense et al. 2013; D'Affonseca et al. 2020; Smith & Carr 2024; Bardot et al. 2025). In geothermal settings, faults exert strong control on heat and fluid transport, functioning either as high-permeability conduits that channel deep, hot fluids or as leakage pathways that reduce reservoir efficiency (e.g., Alt-Epping et al. 2021). Fault behavior is also critical for subsurface storage systems (e.g., for CO_2, H_2, or nuclear waste), where high-permeability fault zones can compromise containment by allowing stored substances to escape, as documented in studies examining CO_2 leakage risks (e.g., Miocic et al. 2019a,b) and in naturally leaking CO_2 faults that serve as analogs for engineered storage sites (Shipton et al. 2004; Lübben & Leven 2018).

Fault zones are also relevant in geotechnical engineering because they may indicate zones prone to hazardous earthquake activity or cause mechanical failure (e.g., Galli et al. 2014; Drahor & Berge

2017; Kruszewski et al. 2022; Gómez-Vasconcelos et al. 2025). Even faults that appear inactive may be reactivated under changing stress conditions driven by natural processes or human activities such as fluid injection (e.g., Caputo et al. 2007; Fazzito et al. 2009; Carreón-Freyre et al. 2016; Naik et al. 2022; Röckel et al. 2022). Therefore, the potential for fault reactivation must be carefully evaluated (e.g., Orellana et al. 2019). In addition to their inherent seismic hazard, fault zones can undergo substantial petrophysical and geotechnical changes driven by fluid–rock interactions, which may promote mineral alteration, dissolution, and precipitation (e.g., Nickschick et al. 2019; Moreira et al. 2025). These processes commonly produce zones of strongly weathered and mechanically weakened rock, increasing susceptibility to geological hazards such as landslides (e.g., Bloom et al. 2022), sinkhole formation (e.g., Fadili et al. 2024; Saribudak & Hawkins 2019; Wang et al. 2025), and deformation or collapse of underground infrastructure such as tunnels (e.g., Ganerød et al. 2006; Rønning et al. 2014; Lesparre et al. 2016).

Across the applications discussed above, it is crucial to determine the spatial location of faults and characterize their mechanical and hydraulic behavior. In this context, understanding near-surface faults involves two principal steps: (1) delineating and describing their geometry, such as position, vertical offset, and dip, and (2) characterizing their petrophysical, hydraulic, and geotechnical properties. The present study primarily focuses on the first aspect. Identifying fault zones in the near surface (top 100 m of the subsurface) is often challenging, as they are rarely exposed and may be ”masked” by recent unconsolidated deposits (e.g., alluvial and colluvial sediments) or modified by weathering and soil-forming processes (e.g., Schütze et al. 2012; Malehmir et al. 2016; Wang et al. 2025).

The location of near-surface faults can sometimes be inferred from surface geomorphology, as faulting can produce characteristic geomorphic features such as linear scarps, triangular facets, aligned springs, or offset drainage patterns (e.g., Audin et al. 2008). However, such features may only be evident in tectonically active regions where they have not been significantly degraded by weathering and erosion or buried by subsequent sedimentation. Even when such geomorphic features are evident in the landscape, they may result from non-tectonic processes such as erosion, sedimentary architecture, or lithological contrasts (e.g., Arnous et al. 2020; León-Loya et al. 2023; Gómez-Vasconcelos et al. 2025). That is, while topography can suggest the possible presence of a fault, it does not provide direct evidence of subsurface fault existence, geometry, or displacement.

Point-based subsurface observations, most commonly obtained from borehole data (logs and cores), are frequently used to infer fault locations. For example, a distinctive stratigraphic unit or clear contact among two units identified across multiple boreholes can be used to constrain the location of a fault and determine its vertical displacement (e.g., Wellmann et al. 2010). However, borehole data are typically sparse, often spaced hundreds to thousands of meters apart, which complicates interpretation.

Additional structural complexities, such as bedding dip, folding, or lateral stratigraphic variations in thickness, can also result in depth changes unrelated to faulting (e.g., Wellmann et al. 2010; Bardot et al. 2025). Therefore, structural reconstructions derived solely from sparse borehole data may yield oversimplified or inaccurate geological models. To overcome these limitations, near-surface geophysical techniques are increasingly combined with borehole information to improve the detection, delineation, and characterization of faults.

Integrating geophysical investigations and borehole information has proven valuable for resolving fault geometry and properties at depth (e.g., Díaz et al. 2014; Lesparre et al. 2016; Barnes et al. 2021). Electrical resistivity tomography (ERT), seismic refraction tomography (SRT), and gravity surveys, among others, have proven effective in imaging the geoelectrical and mechanical contrasts related to faults (Vanneste et al. 2008; Ronczka et al. 2017; Nickschick et al. 2019; Menzel et al. 2024; Giraud et al. 2024). Time-lapse geophysical studies have also been used to investigate fluid flow along faults, most commonly through repeated ERT or electromagnetic imaging, demonstrating the value of combining temporal data with wells or hydrogeological modeling to interpret fault-controlled flow processes (e.g., Torrese & Pilla 2021; Gonzalez-Duque et al. 2024; Balza-Morales et al. 2025). Less commonly, gas sampling (e.g., Schütze et al. 2012; Zarroca et al. 2012; Léger et al. 2025) and temperature measurements (e.g., Hess et al. 2009) have been included to further constrain fault activity and fluid circulation.

Although geophysical methods are valuable tools for investigating faults, several important aspects must be considered: Malehmir et al. (2016) and Gao & Wellmann (2025) raise concerns that interpretations of geophysical data (even when multiple datasets are available) should be regarded as speculative in the absence of direct observations. Nguyen et al. (2007), Ronczka et al. (2017) and Nickschick et al. (2019) caution that smoothness-constrained inversion results may obscure or fail to detect faults. In this context, an emerging alternative to traditional grid-based parameterization used in smoothness-constrained inversion methods is layer-based model parameterization (e.g., Arboleda-Zapata et al. 2022b). In this approach, the parameterization of faults and lithological boundaries can be explicitly incorporated into the inversion process to improve structural resolution, particularly when sharp contrasts are expected (e.g., Arboleda-Zapata et al. 2025a). The approach is particularly convenient for structurally constrained joint-inversion methods of two or more collocated geophysical data sets, where the preferred models are those that fit the joint data sets while keeping a common or similar structure, e.g., by coinciding interfaces. Such joint strategies can reduce model ambiguity and result in more realistic model solutions (Wagner & Uhlemann 2021).

In addition to field-based investigations, synthetic modeling has become a crucial tool for assessing the capabilities and limitations of geophysical inversion techniques. Early work by Olayinka &

Yaramanci (2000) examined the ability of a block inversion algorithm to identify sharp resistivity contrasts, providing initial benchmarks for fault detection.

Zhou et al. (2014) proposed an image-guided inversion of ERT data to enhance the expected sharp boundaries by considering structural constraints, using, for example, a seismic reflection image. In the context of SRT, Chen & Zelt (2016) applied frequency-dependent travel-time tomography and full-waveform inversion to resolve the velocity contrast of a synthetic model depicting a fault zone. Building on a similar synthetic model of the last authors, Hellman et al. (2017) developed a joint-inversion approach that combined ERT and SRT data, relying on cluster-based model integration. Tso et al. (2021) employed an Ensemble-Kalman-Inversion approach to image a model that mimics a geological fault and quantify model uncertainties. More recently, machine-learning techniques, typically based on artificial neural networks, have shown promise in mitigating the smoothing effects of conventional inversion and improving the detectability of sharp geological boundaries (e.g., Jiang et al. 2018; Kong et al. 2023; Zhang et al. 2025).

In this study, we present a workflow for joint inversion of ERT and SRT data, targeting subsurface models where a geological fault is expected. The approach combines a layer-based model parameterization with a global optimization algorithm to recover fault geometry and layer properties (e.g., resistivity and P-wave velocity), which are consistent with the observed data. The strategy is flexible, allowing adaptive mesh refinement along faults and other interfaces to improve the accuracy of the forward response of sharp, layered models. By explicitly incorporating the fault structure and layers during inversion, the method reduces the ambiguity and bias when interpreting faults and other sharp interfaces in comparison to standard smoothness-constrained inversion. Additionally, to address the inherent non-uniqueness of geophysical inversion, we explore the landscape of the objective function by considering different prior models and trade-off parameters of the objective function. In this way, model solutions with comparable data misfits are treated as plausible subsurface scenarios. The framework is readily extendable to other geophysical methods and can guide the selection of optimal borehole and trench locations for ground-truthing and further investigations. The latter would help discard incompatible solutions and identify the most likely structure among the plausible solutions suggested by geophysical surveying and inversion.

2 METHODOLOGY

This section briefly reviews surface ERT and SRT methods, emphasizing their complementarity. More detailed theoretical background is given by Binley & Slater (2020) for ERT and by White (1989) and Watts et al. (2023) for SRT, among others. We then describe our parameterization and inversion strategy. Specific procedures for processing and inversion of each data set are summarized in the corresponding results sections.

2.1 Principles of ERT and SRT

In ERT surveys, electrical current is typically injected through a pair of electrodes (current electrodes A and B), and the resulting voltage is measured between another pair (potential electrodes M and N). This four-electrode setup (A, B, M, and N), referred to as a quadrupole, is arranged according to a chosen array configuration (e.g., dipole–dipole, Wenner–Schlumberger, multigradient). Collecting measurements from multiple quadrupoles along a profile produces a set of apparent resistivities, which are commonly displayed as 2-D pseudo-sections. The array type and electrode spacing strongly influence the depth of investigation, coverage, and sensitivity patterns (e.g., Furman et al. 2003). Thus, combining multiple array configurations can improve spatial resolution (e.g., Bezerra-Guedes et al. 2022; Arboleda-Zapata et al. 2025b).

In SRT, seismic energy is typically generated by a hammer strike or weight drop on a metallic plate, and geophones record the resulting ground motion as seismic waves propagate through the subsurface. In the field example shown later, we utilize a seismic source whose recorded signal exhibits a dominant frequency of approximately 100 Hz, and geophones with a natural frequency of 10 Hz that are sensitive to vertical ground motion and are thus well-suited for capturing first arrivals of compressional body waves, denoted as P-waves. Throughout this work, "velocity" specifically refers to P-wave velocity. In the near surface, where velocities are typically below 1000 m/s, this corresponds to wavelengths on the order of 10 m, whereas for deeper layers with velocities between 2000 and 4000 m/s, the corresponding wavelengths are on the order of 20–40 m. Based on the quarter-wavelength criterion (e.g., Bailly et al. 2019; Léger et al. 2025), this implies a theoretical vertical resolution on the order of 2.5 m in the near subsurface and 5–10 m at larger depths. The collection of traces from all geophones for one source point is called a shot gather. Similar to ERT, acquiring shot gathers at different source positions along a 2-D survey line can enhance data coverage and better reveal lateral and vertical variations of features. During data processing, the first-arrival times are picked from all shot gathers.

After collecting and processing the ERT and SRT data, the apparent resistivities and first-arrival times are inverted to obtain models of resistivity and velocity distributions, respectively. Inversions aim to find a model that reproduces the observed data within their estimated or assumed errors while honoring any prior information (e.g., Arboleda-Zapata et al. 2025b). While ERT is primarily sensitive to water content, salinity, porosity, grain-size distribution, and temperature (e.g., Binley & Slater 2020), SRT is sensitive to the elastic properties (bulk and shear modules) and density of the subsurface, which in turn depend on factors such as compaction, porosity, saturation, and sediment/lithological fabric (e.g., Clair et al. 2015). Therefore, ERT and SRT are complementary geophysical techniques for imaging structural features and petrophysical properties of the subsurface.

Because ERT and SRT are sensitive to different physical properties and have different resolutions, cooperative interpretation or joint inversion approaches can characterize the subsurface more completely (e.g., Wagner & Uhlemann 2021). In cooperative interpretation, models obtained by both methods are compared to identify complementary or contrasting features (e.g., Schütze et al. 2012; Léger et al. 2025). For example, in a two-layer system with high resistivity contrast and a similar elastic properties, ERT may resolve both layers, whereas SRT images them as a single unit. Conversely, if the layers differ in compaction and stiffness but have similar resistivity, SRT can distinguish between them, whereas ERT cannot. In the ideal case, the layers contrast in both resistivity and velocity, allowing both methods to resolve them and thereby increasing confidence in the interpretation. In joint inversion, the datasets are structurally and/or petrophysically coupled, allowing the inversion process to exploit the complementary sensitivities of each method and thereby improving model reliability (e.g., Wagner & Uhlemann 2021; Jordi et al. 2020).

2.2 Parameterization and Inversion Strategy

In this study, we consider a layer-based model parameterization (LBMP) where parameters are updated using Particle Swarm Optimization (PSO). Our approach builds upon the work of Arboleda-Zapata et al. (2022b,a), who demonstrated the potential of combining LBMP and PSO for inverting layered systems as typically present in coastal aquifers and subsea permafrost. The latter framework mainly focused on resolving continuous interfaces along a profile. In this study, we extend the framework by (1) allowing the explicit representation of faults, and (2) enabling the joint inversion of collocated 2-D ERT and SRT datasets. Our model parameterization uses a limited number of parameters to represent both geometry and physical properties (e.g., resistivity or velocity). This approach naturally yields simplified models, which may help accelerate convergence rates in global inversion algorithms such as PSO.

2.2.1 Layer-Based Model Parameterization with Faults

Our model parameterization is designed to represent both fault geometry and geological layers in the near subsurface. In the model, a fault is defined as a structural discontinuity that offsets layered units with distinct resistivity and velocity in each layer. Together, the fault and layers define the structure of the subsurface. In this study, we restrict the analysis to cases with a single fault and horizontal layering, where the latter is typical for many sedimentary sequences (e.g., Sana et al. 2021; Menzel et al. 2024) and weathered crystalline terrains (e.g., Giao et al. 2008; Chen & Niu 2022).

The parameterization of the model begins with defining the parameters that represent the fault in the model domain. The fault position is described by the horizontal coordinates of two nodes: one at the topographic surface (upper boundary) and the other at the maximum investigation depth (lower boundary) of the model domain. Allowing both nodes to vary within the same horizontal range enables the fault to dip in either direction. After defining the fault structure, interfaces are introduced to delimit homogeneous layers on both sides of the fault. Each layer is assumed to have uniform resistivity or velocity.

In our LBMP, each layer is bounded by two interfaces, which may include the land surface or the model base. In contrast to other interfaces, the vertical positions of the latter two boundaries are fixed and are thus not treated as model parameters. If n_i internal interfaces (excluding the top and base) are defined on each side of the fault, the geometry requires $2(n_i+1)$ parameters and the physical properties (resistivity or velocity), another $2(n_i+1)$, giving a total of $4(n_i+1)$ parameters for a single dataset. For joint inversion of ERT and SRT data using a common mesh, an additional $2(n_i+1)$ parameters are introduced, resulting in $6(n_i+1)$ parameters in total. For example, a model with three interfaces ($n_i = 3$) on each side of the fault results in 24 model parameters.

After constructing the model geometry and assigning homogeneous layer properties, the parameterization is mapped onto an unstructured triangular mesh, which is then used for forward simulations. These simulations are performed with the open-source library pyGIMLi (Rücker et al. 2017), which handles mesh generation internally using the Triangle library (Shewchuk 1996). Triangle produces 2-D unstructured meshes well suited for incorporating topography and local refinements, e.g., along faults, interfaces, or between sensors (electrodes / geophones).

Prior geological knowledge can be incorporated to constrain the model. This may refer to the depths of interfaces, the fault type (e.g., normal or reverse), or lithological information on either side of the fault. When such information is limited, fault location, layer thicknesses, and property values are allowed to vary independently. Even when geology appears similar across the fault, caution is advised because groundwater flow, weathering, and other processes may cause the same geological unit to exhibit different resistivity or velocity values on either side of the fault (e.g., Nickschick et al. 2019; Menzel et al. 2024). In addition to geological priors, smoothness-constrained (deterministic) inversion results can provide valuable constraints, particularly in the shallow subsurface where data sensitivity and resolution are the highest. Velocity or resistivity values derived from these inversions can be fixed or restricted within realistic ranges, thereby reducing model ambiguity while preserving flexibility in deeper layers.

In collocated ERT and SRT profiles, when the electrode and geophone layouts differ in position or overall profile length (as in our field example), constructing a single mesh for both datasets can lead to inefficient and unstable discretization. For example, extending the mesh of a shorter survey to match the length of a longer one enlarges the model domain unnecessarily, increasing the total number of unknowns and the computational cost. Additionally, because electrode and geophone positions may not coincide exactly (due to differing spacings, different starting references, or GPS uncertainty), merging all sensor positions into a single mesh can result in near-coincident surface nodes causing excessive and unnecessary mesh refinement, further increasing computation time and memory requirements. To avoid these issues, as illustrated in our field example, we generate separate meshes for the ERT and SRT datasets while maintaining an almost identical model geometry across both meshes. Furthermore, for numerical accuracy, we extend the model boundaries by at least two profile lengths for ERT, and by half a profile length for SRT, reflecting the broader spatial sensitivity of electrical potential fields compared to the more localized sensitivity of seismic ray paths (e.g., Reynolds 2011).

To validate that our discretization strategy consistently produces high-quality meshes across a wide range of fault scenarios and ensures numerical stability in forward simulations, we performed extensive tests with randomly generated meshes and model parameters. For example, in the two randomly generated meshes in Figs. 1a and d, it is noticeable that the refinements are on the top of the model domain (i.e. where the sensors are placed) and along the fault. Figs. 1b-c and e-f illustrate how the same mesh is used to assign different model parameters (i.e. velocity and resistivity). The tests demonstrated mesh stability across randomly generated models, indicating that the approach remains reliable under small parameter updates and is well-suited for the subsequent inversion step.

2.2.2 *Particle Swarm Optimization*

The PSO algorithm was originally introduced by Kennedy & Eberhart (1995) as an analogy of the collective behavior of a swarm of birds and has since been used in multiple geophysical applications (e.g., Arboleda-Zapata et al. 2022b; Abril et al. 2022). In PSO, a swarm of ”particles”, each representing a model within the parameter space, explores different areas of the landscape of the objective function until converging toward the global or a local minimum. The motion of the particles is influenced by three factors: an inertia term that preserves part of its previous velocity, a cognitive component that reflects the memory of its best position, and a social component that represents the attraction toward the best position found by the swarm. Considering these terms, the velocity and position of the particles are updated as follows:

$$v_i^{k+1} = wv_i^k + c_1 r_1^{k+1}(m_i^l - m_i^k) + c_2 r_2^{k+1}(m^g - m_i^k), \tag{1}$$

$$m_i^{k+1} = m_i^k + v_i^{k+1}, \tag{2}$$

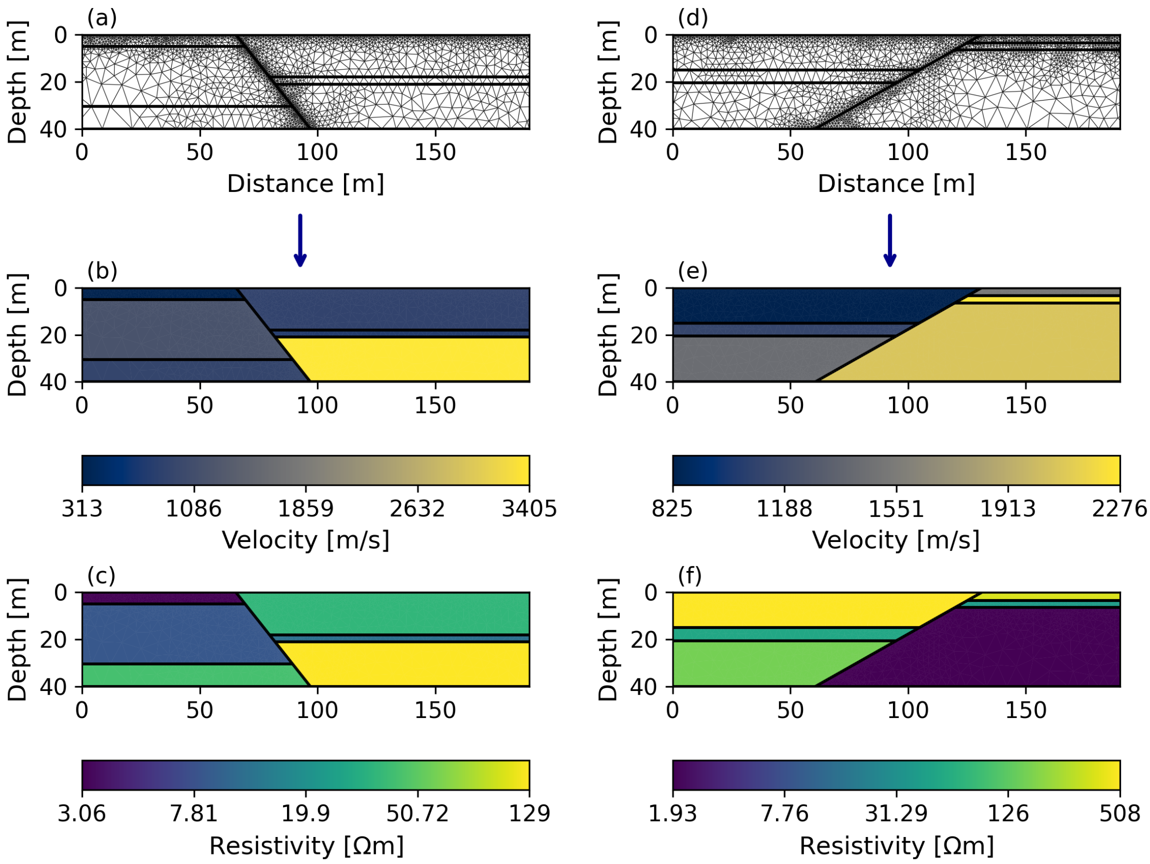

Figure 1. Randomly generated finite-element unstructured meshes and model assignments. Panels (a) and (d) show two meshes, while panels (b–c) and (e–f) display the corresponding velocity and resistivity models assigned to meshes (a) and (d), respectively, using homogeneous layer values.

where v_i^k denotes the velocity of particle i at iteration k; m_i^k is its current position in the model space; m_i^l is the best position found by that particle (local best); and m^g is the best position found by the entire swarm (global best). The constants w, c_1, and c_2 control the influence of the inertia, cognitive, and social components, respectively. Following Tronicke et al. (2012), we set $w = 0.73$ and $c_1 = c_2 = 1.5$. The random coefficients r_1 and r_2 are drawn from the standard uniform distribution, introducing stochastic variability that enhances exploration of the model space and helps avoiding convergence to a poor local minimum. In addition, the number of particles and the maximum number of iterations (or an alternative stopping criterion) must be defined. These were determined empirically through preliminary test runs, during which we examined the convergence history and resulting models to identify values that led to similar misfit values across runs with different randomly generated starting models. Note that we refer to a run as one complete inversion cycle from the first iteration until a stopping criterion is met.

2.2.3 Joint Inversion Strategy

Fig. 2 presents the overall workflow for the joint inversion of collocated ERT and SRT data using the PSO algorithm. First, the ERT and SRT datasets are prepared. Next, the model parameters and their lower and upper bounds are defined, typically based on available prior information. When prior knowledge is limited, these bounds must be chosen more broadly. These parameter bounds are then used to randomly generate sets of parameter combinations (particles), used to construct the initial resistivity and velocity models. Forward responses are computed for each model, and data misfits are calculated by comparing simulated and observed datasets. The misfits are combined into a weighted joint objective function that quantifies the overall misfit for each particle (explained in more detail below). The particle velocities and positions are then updated according to Eqs. 1 and 2. This procedure iterates until the stopping criterion (e.g., a maximum number of iterations or a target misfit) is reached. The resistivity and velocity models corresponding to the lowest joint misfit are saved as the best result for that PSO run. To identify alternative model solutions that fit the data equally well, the entire inversion process is repeated multiple times, producing an ensemble of best-fitting models.

In the following, we describe several aspects of our workflow that influence the performance and stability of the joint inversion in more detail. During each inversion run, the number of interfaces in the model is kept constant. Preliminary tests indicated that reliable convergence was achieved when using up to five interfaces. Increasing the number of interfaces to numbers beyond five often caused convergence at an early stage to local minima characterized by higher data misfits. The initial models (i.e. particles at the first iteration) represent geological layers that already include a structural discontinuity, either a fault (with displacement) or a joint (without evident relative displacement). This is in contrast to conventional smoothness-constrained inversion approaches, which typically employ a starting model that is homogeneous or shows a constant gradient. Mesh generation is adaptive, ensuring that a new mesh is created for each particle in every iteration to more accurately capture changes in fault geometry and layer-interface depth.

Because areas affected by faults tend to exhibit complex variations in physical properties, our simplified layered approach may yield relatively large data misfits compared to deterministic inversions. To compensate for this, we propose two complementary strategies. First, the model parameters in the upper few meters can be fixed using values derived from smoothness-constrained inversions, which typically provide reliable estimates in the shallow subsurface, where data sensitivity is highest. After fixing the near-surface parameters, the LBMP inversion can focus on exploring deeper homogeneous layers and fault-related features.

To jointly invert the SRT and ERT data, we define the objective function ϕ that includes misfit terms for SRT (ϕ_{srt}) and ERT (ϕ_{ert}):

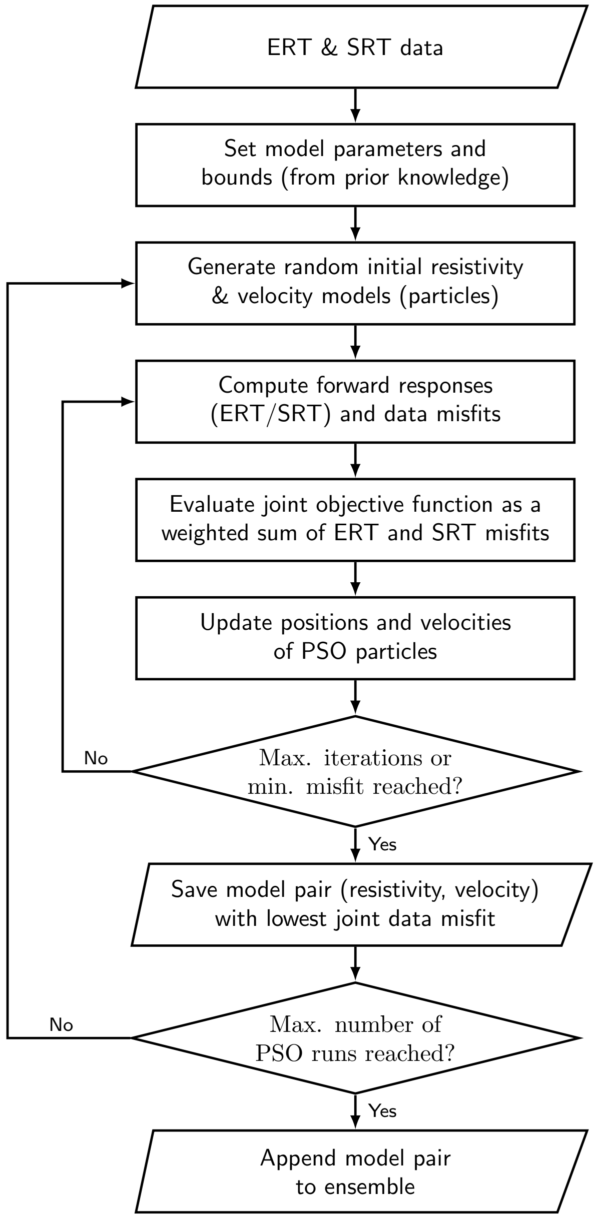

Figure 2. Workflow for joint inversion of ERT and SRT data.

$$\phi = w_{\text{srt}}\,\phi_{\text{srt}} + (1 - w_{\text{srt}})\,\phi_{\text{ert}}, \tag{3}$$

where w_{srt} is a trade-off parameter that balances the relative influence of each term in the objective function. Note that for values of w_{srt} greater than $1/2$, greater emphasis is placed on the misfit term associated with the SRT data. To compute the misfit terms in Eq. 3, we evaluate the relative error for ϕ_{srt} and the logarithmic difference for ϕ_{ert} as follows:

$$\phi_{\mathrm{srt}} = \frac{1}{\sqrt{n}} \left\| \frac{\mathbf{t}^{\mathrm{sim}} - \mathbf{t}^{\mathrm{obs}}}{\mathbf{t}^{\mathrm{obs}}} \right\|_2 , \tag{4}$$

$$\phi_{\mathrm{ert}} = \frac{1}{\sqrt{n}} \left\| \log_{10}(\rho_a^{\mathrm{sim}}) - \log_{10}(\rho_a^{\mathrm{obs}}) \right\|_2 , \tag{5}$$

where $\mathbf{t}^{\mathrm{sim}}$ and $\mathbf{t}^{\mathrm{obs}}$ denote the simulated and observed first-arrival travel times, respectively. Similarly, ρ_a^{sim} and ρ_a^{obs} represent the simulated and measured apparent resistivities, respectively. Note that all operations are performed element-wise.

Note that $w_{\mathrm{srt}} = 1/2$ would not necessarily imply that both datasets contribute equally to the objective function. Because the underlying physics (along with factors such as noise levels, data coverage, and target properties) of the two methods differ, the optimization may progress at different rates. As a result, unequal weights may be required to prevent the joint inversion from being dominated or misled by a single dataset. In practice, testing a range of weighting combinations may be necessary to identify a stable and balanced joint inversion.

We based the use of different misfit terms for ERT and SRT on preliminary tests that showed that the logarithmic difference of resistivity accelerates convergence, which is consistent with resistivity behaving as a logarithmic parameter (e.g., Wheelock et al. 2015; Arboleda-Zapata et al. 2022b). Conversely, using the relative difference on a linear scale for SRT data makes sense because first arrival times behave as a linear parameter (e.g., White 1989). Both misfit terms are expressed in relative form, which effectively normalizes them. Thus, summing the two normalized terms in Eq. 3 yields a meaningful scalar objective function which is convenient for joint inversion (e.g., Tronicke et al. 2011).

In this study, we considered no explicit data error estimates to weight the ERT and SRT residuals, implying that each data point contributes equally to the objective function. While we acknowledge the significance of exploring various error models during the inversion process (e.g., Tso et al. 2017; Arboleda-Zapata et al. 2025b), exploring such procedures would lie beyond the scope of the present work.

2.2.4 Smoothness-Constrained Geometry-Preserving Inversion

In a second inversion step, the interfaces and model parameters obtained from the LBMP approach are used as starting and/or reference models for subsequent smoothness-constrained inversions, in which the interfaces are explicitly incorporated as structural constraints (e.g., Bergmann et al. 2014; Fischer et al. 2016; Wunderlich et al. 2018; Jiang et al. 2020). Here, the inversion is performed independently for SRT and ERT. A layered model obtained from our LBMP approach serves as an informed initial guess, guiding the deterministic inversion toward a solution in the vicinity of the layered model. At the same time, the explicit incorporation of interfaces can be used to prevent coupling across their boundaries and restrict smoothing to be applied within individual zones. When the layered model is also used as a reference model, the inversion is damped toward this solution, limiting deviations from the previously identified parameter values within the layers. Overall, this inversion framework guides the inversion toward structurally consistent models that remain close to the found layered model while likely improving data misfit through the introduction of heterogeneity within each distinct zone. Following Bergmann et al. (2014), the objective function ϕ_{sc} for the smoothness-constrained geometry-preserving inversion reads as follows:

$$\phi_{\mathrm{sc}} = \phi_{\mathrm{d}} + \lambda\, \phi_{\mathrm{m}}, \tag{6}$$

$$\phi_{\mathrm{sc}} = \left\|\mathbf{W}_{\mathrm{d}}\left(\mathbf{d}_{\mathrm{obs}} - \mathbf{f}(\mathbf{m})\right)\right\|_2^2 + \lambda\, \left\|\mathbf{W}_{\mathrm{m}}\, \mathbf{C}\, \mathbf{W}_{\mathrm{c}}\,(\mathbf{m} - \mathbf{m}_0)\right\|_2^2 \tag{7}$$

where ϕ_{d} is the data misfit term and ϕ_{m} is the model-roughness term, whose relative contributions are balanced by the regularization parameter λ. The vectors $\mathbf{m}$ and $\mathbf{m}_0$ denote the model parameters (here, resistivities or velocities of all elements of the computational mesh) and the corresponding starting or reference model, respectively. In this study, $\mathbf{m}_0$ is derived from the joint inversion results obtained using the LBMP approach. The vector $\mathbf{d}_{\mathrm{obs}}$ contains the observed ERT or SRT data, and $\mathbf{f}(\mathbf{m})$ represents the response of the forward operator applied to $\mathbf{m}$. The data-weighting matrix $\mathbf{W}_{\mathrm{d}}$ is constructed under the assumption of Gaussian-distributed measurement errors. The derivative matrix $\mathbf{C}$ represents first-order differences between neighboring model cells and thus encodes spatial smoothness. The constraint-weight matrix $\mathbf{W}_{\mathrm{c}}$ incorporates structural information by modifying or suppressing the coupling across selected boundaries, such as layer interfaces or faults, thus controlling the degree of smoothing across these interfaces. In the particular case where the diagonal entries of $\mathbf{W}_{\mathrm{c}}$ corresponding to these boundaries are set to zero (as considered in this study), smoothing is applied exclusively within structurally defined zones, while sharp parameter contrasts are allowed across their boundaries. The model-control matrix $\mathbf{W}_{\mathrm{m}}$ allows additional weighting of the roughness constraint, for example, to account for anisotropic smoothing or depth-dependent regularization. Additionally, larger values of λ enforce stronger regularization and therefore yield models that remain closer to the chosen starting and reference models.

3 RESULTS

In this section, we demonstrate the performance of the proposed joint inversion approach using a synthetic test case and field data sets. The synthetic example is designed to evaluate the ability of our workflow to recover a known subsurface structure under controlled conditions (e.g., perfect sensor–ground coupling), whereas the field example illustrates its applicability to real data, which typically involves additional challenges and complexities.

3.1 Synthetic Example

Fig. 3 shows the synthetic velocity and resistivity models used in this study. Both models share the same geometry, consisting of three horizontal layers displaced by a normal fault with a vertical offset of 8 m. In the velocity model (panel a), the upper, middle, and lower layers have values of 500 m/s, 1500 m/s, and 3000 m/s, respectively, while the corresponding resistivities in panel (b) are 10 Ωm, 200 Ωm, and 60 Ωm. Note that the velocity model exhibits a monotonic increase with depth, while the resistivity model is non-monotonic, presenting a more resistive intermediate layer. The geometry and model parameters resemble a simplified scenario, where the middle layer with intermediate velocity and high resistivity may be interpreted as a coarse-grained sediment over- and underlain by finer-grained, less resistive layers. The coarse-grained layer may serve as an aquifer. In a real system, a fault displacing and disconnecting such an aquifer would have significant implications for groundwater flow and solute transport, but here the configuration serves primarily as a structurally realistic test case for evaluating our inversion workflow.

To generate synthetic SRT and ERT data, 96 collocated sensors (geophones and electrodes) were positioned along the profile with a uniform spacing of 2 m. We simulated the synthetic measurements for both SRT and ERT using the respective forward solvers implemented in pyGIMLi (Rücker et al. 2017). SRT travel times were simulated using a Dijkstra-based ray-tracing algorithm. For ERT, apparent resistivities were simulated using a combination of dipole–dipole and multi-gradient electrode configurations, selected for their complementary sensitivities to horizontal and vertical resistivity variations, respectively (e.g., Comte et al. 2012; Arboleda-Zapata et al. 2025b). To mimic realistic field conditions, Gaussian noise with relative standard deviations of 3% and 4% was added to the simulated travel times and apparent resistivities, respectively.

To jointly invert the synthetic ERT and SRT data, we followed the strategy outlined in Sec. 2.2.3 and assigned equal weights to the ERT and SRT misfit terms (i.e. $w_{\text{srt}} = 1/2$ in Eq. 3). Additionally, we assumed a three-layer structure with the profile intersecting a fault, although the exact location of the fault along the profile was treated as unknown. To evaluate how different levels of prior knowledge influence the results of joint inversion, we considered three scenarios corresponding to different levels of prior knowledge. The first scenario represents the case with the largest degree of freedom, where no additional information was provided beyond these general assumptions. In the second and third scenarios, the interface depths were assumed to be known on the right side of the fault and on both sides of the fault, respectively. A tolerance of ± 0.5 m was allowed for each assumed interface depth to

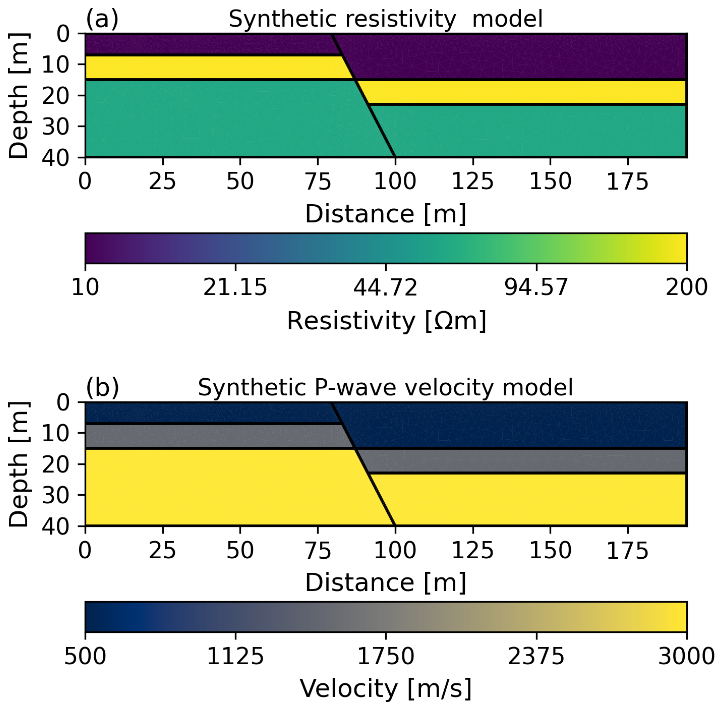

Figure 3. Synthetic model used in this study. Panel (a) shows the velocity model and panel (b) the resistivity model; both share the same geometry, consisting of three horizontal layers displaced by a normal fault with an 8 m vertical offset that fully separates the middle layer.

account for possible measurement or interpretation errors, as commonly expected in drilling surveys at these relatively shallow depths. This tolerance can be fine-tuned depending on sampling type, depth, and operator experience. In the end, for each scenario, 100 models were generated, and the six best models with respect to the lowest values of the combined data misfit (Eq. 3) are shown and discussed below.

Figs. 4a-l show six joint-inversion results with the lowest misfits for Scenario 1, where no prior information was provided about the depth of the interfaces. The data misfits for these six models range from $5.60-5.91\%$ for ϕ_{ert} and from $5.46-5.63\%$ for ϕ_{srt}. The horizontal position of the fault at shallow depths is well resolved in all cases. However, several models (e.g., panels d and e) exhibit increasing disagreement in the fault position with depth. The interfaces on the left side of the fault are generally better constrained than those on the right side, which show greater variability. Notably, the resistivity of the middle layer tends to be underestimated in most cases, reflecting a trade-off between layer thickness and resistivity: where the recovered middle layer is thicker than in the synthetic truth, its resistivity is correspondingly lower. We also want to highlight that in panels (e and k) the fault dips

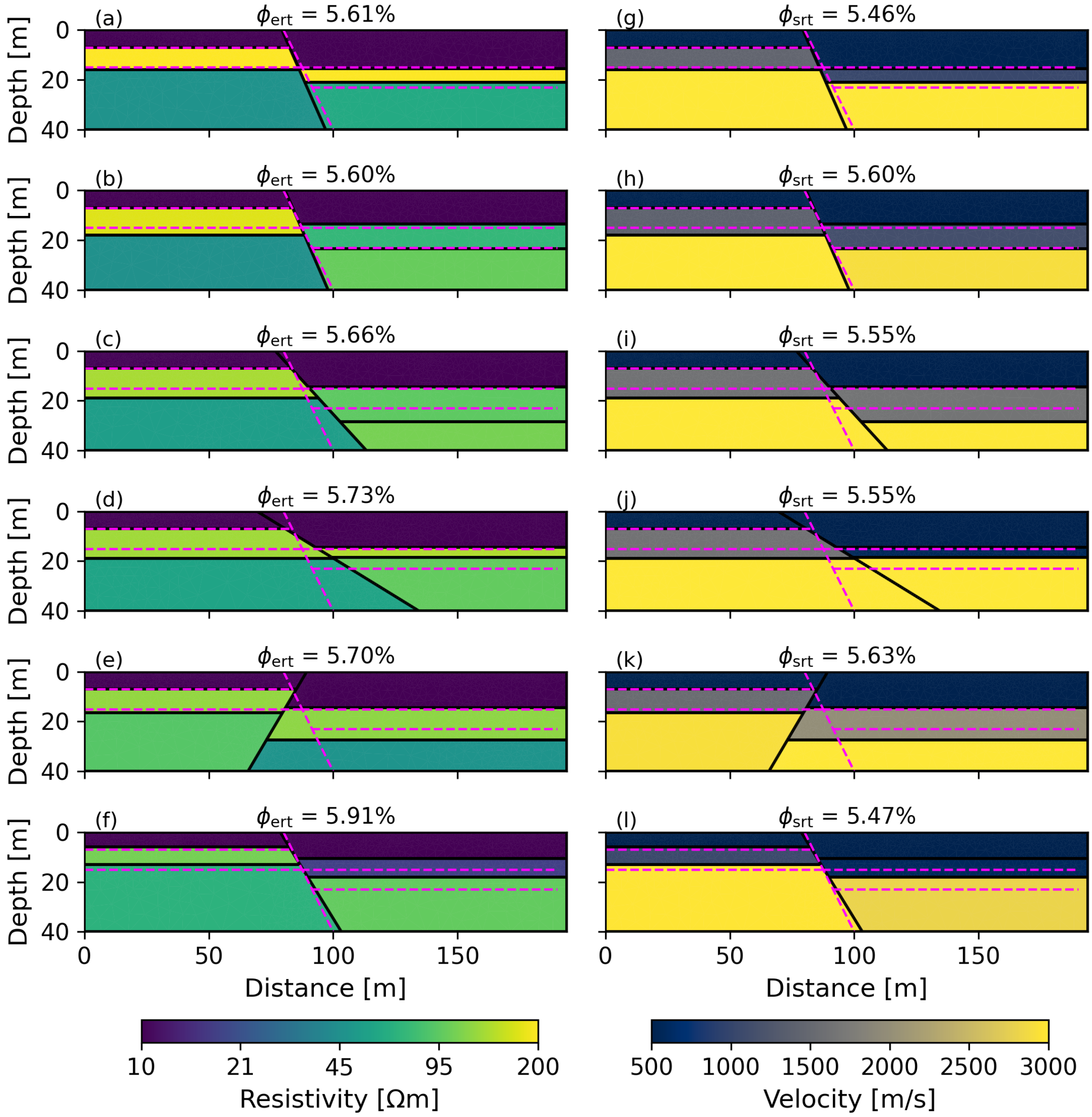

Figure 4. Joint inversion results for Scenario 1, with no prior information on interface depths. Panels (a–f) show the resulting resistivity models, and panels (g–l) show the corresponding seismic-velocity models. The magenta dashed lines indicate the interfaces and fault location from the synthetic reference model. The values of the objective functions are shown at the top of each panel.

toward the left, resembling a reverse fault, while panels (f and l) display a nearly two-layer structure in both ERT and SRT results, despite achieving comparable misfit values.

Figs. 5a–l show the six joint inversion results with the lowest misfits for Scenario 2, where interfaces between layers on the right side of the fault were assumed to be known. The corresponding data misfits range from 5.58 – 5.72% for ϕ_{ert} and from 5.40 – 5.50% for ϕ_{srt}. Similarly to Scenario 1, the horizontal position of the fault near the surface is almost perfectly resolved in all models, although some deviations are observed at greater depths, particularly in panels (d–f), where the fault dips towards the left, depicting a reverse fault. Overall, the resistivity and velocity values are in better agreement with the synthetic model than in Scenario 1. The constrained side of the model shows a significant improvement in resolving layer properties, particularly in the velocity models, which in all cases successfully recover the three expected layers. By contrast, the unconstrained side still exhibits moderate variability. In addition, compared to Scenario 1, more models recover the resistivity of the middle layer closer to its true value. There are also informative distinctions: for example, panels (a) and (c) display a two-layer resistivity structure on the right side of the fault, whereas the corresponding seismic models in panels (g) and (i) still capture a distinct velocity contrast. It is worth noting that, although the models in panels (d–f) display a reverse-fault geometry, their data misfits are comparable to those in panels (a–c), which are the ones in better agreement with the synthetic truth.

Figs. 6a–l show the six joint inversion results with the lowest misfits for Scenario 3, where the interfaces between layers on both sides of the fault were assumed to be known. The corresponding data misfits range from $5.49-5.72\%$ for ϕ_{ert} and from $5.40-5.51\%$ for ϕ_{srt}. As in Scenarios 1 and 2, the position of the fault at the surface is well resolved in all models, although deviations in fault dip are still evident as seen in panels (e) and (f). The resistivity and velocity values for the different layers show a strong correspondence with the synthetic reference model (see Fig. 3), representing a clear improvement over Scenarios 1 and 2. Despite these improvements, the resistivity model in panel (f) still displays a two-layer structure on the left side of the fault and even suggests a reverse fault geometry.

As shown in Figures 4–6, in some cases either the ERT or SRT result exhibits a two-layer structure; however, when this occurs, the complementary method is typically able to resolve the three-layer structure. This highlights how collocated ERT and SRT data contribute to a more reliable subsurface characterization. Even when including additional constraints, some models still result in a reverse-fault geometry while achieving misfit values comparable to those obtained for the correct fault configuration (Fig. 3). This indicates that models exhibiting a reverse fault configuration belong to the space of acceptable model solutions, and that additional prior information would be required to select the geologically most plausible model among these competing scenarios.

As shown in Table 1, the three scenarios highlight improved convergence of the joint inversion results toward the true fault geometry and layer parameters as structural information is gradually incorporated. For example, the ability of the models to reproduce the fault location within 5 m at the surface and 10 m at the bottom (40 m depth) increases progressively from Scenario 1 to Scenario 3. A similar trend is observed for the estimation of layer interfaces and physical properties. When considering models whose interface depths fall within a tolerance of ± 2 m for the shallowest left interface and

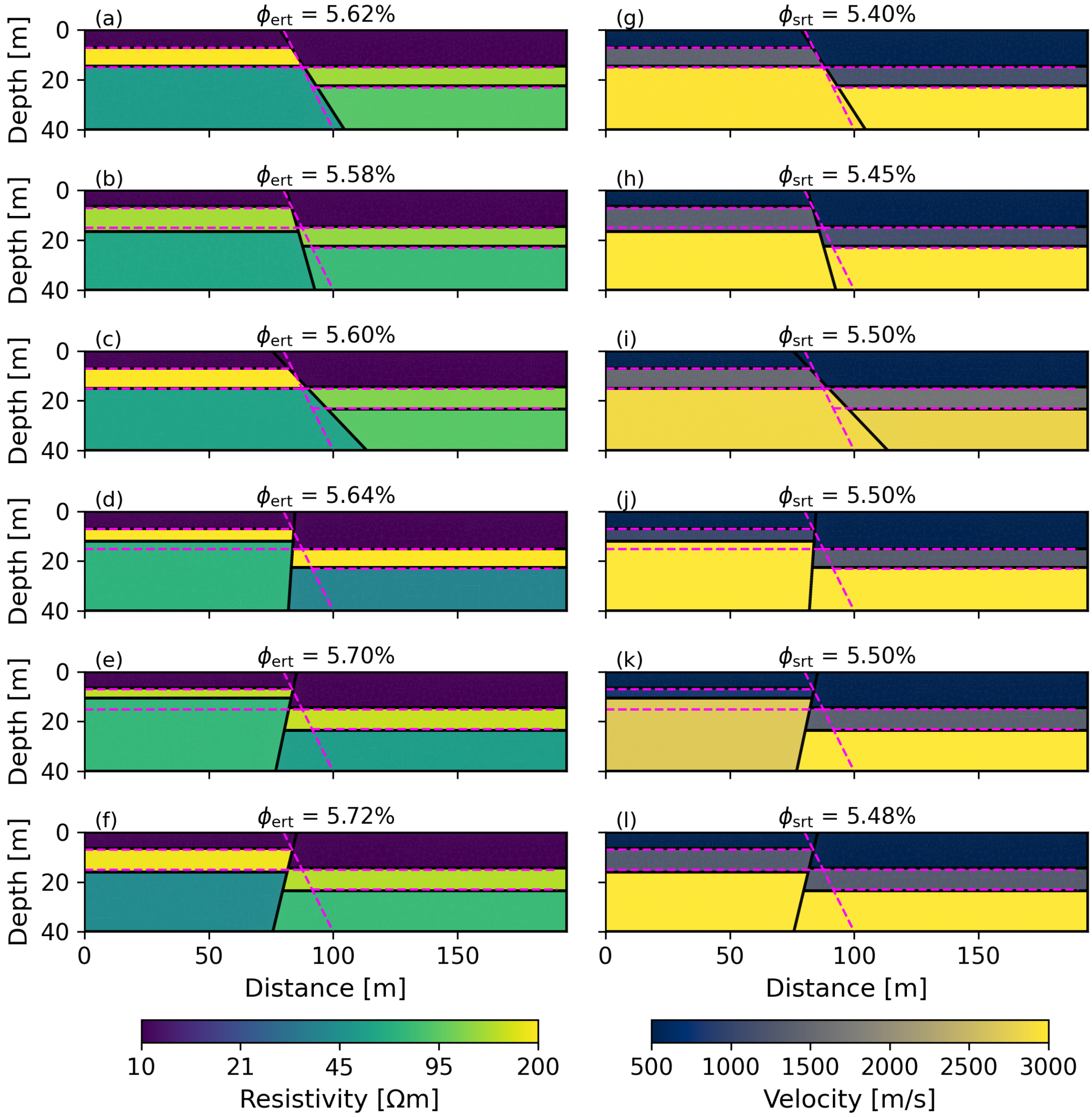

Figure 5. Joint inversion results for Scenario 2, with no prior information on interface depths. Panels (a–f) show the resulting resistivity models, and panels (g–l) show the corresponding seismic velocity models. The magenta dashed lines indicate the interfaces and fault location from the synthetic reference model. The values of the objective functions are shown at the top of each panel.

± 3 m for the deeper interfaces (to account for decreased sensitivity with depth), and whose resistivity and velocity values are resolved within 15% of the true values (in linear scale), the number of models consistent with the true parameters increases from Scenario 1 to Scenario 3. Note that although the left side of the model is unconstrained in Scenarios 1 and 2, the structural constraints introduced on the right side in Scenario 2 result in improved parameter estimation on the left side of the model, as indicated by the increased number of models in Scenario 2 that converged to the true parameter value

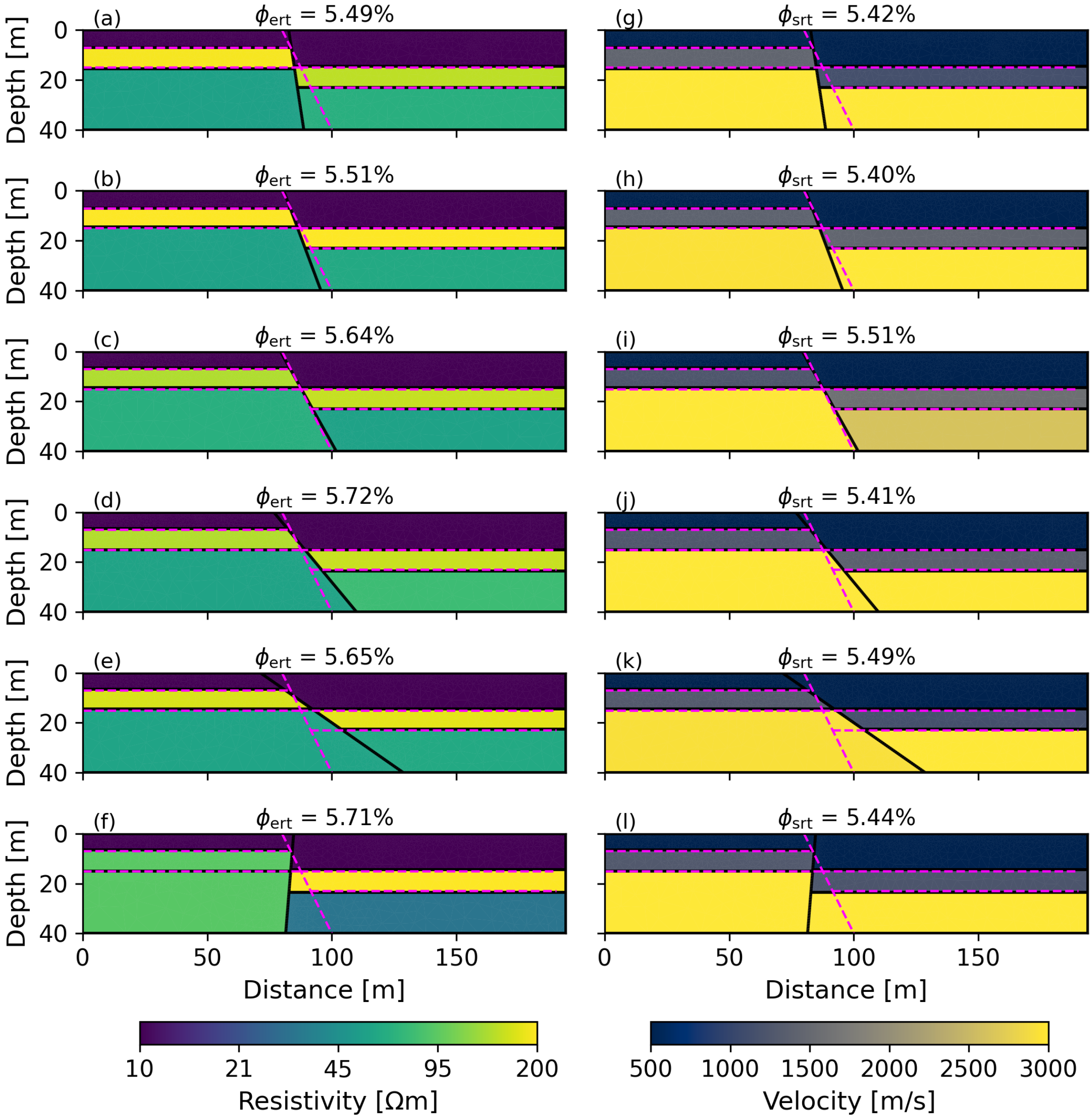

Figure 6. Joint inversion results for Scenario 3, with no prior information on interface depths. Panels (a–f) show the resulting resistivity models, and panels (g–l) show the corresponding seismic velocity models. The magenta dashed lines indicate the interfaces and fault location from the synthetic reference model. The values of the objective functions are shown at the top of each panel.

on the left side of the fault. This indicates that introducing structural constraints on one side of the fault can enhance parameter recovery on the opposite side.

3.2 Field Example

To further test the performance of the proposed joint inversion workflow under real-world conditions, we applied it to ERT and SRT data collected in central France by Léger et al. (2025) near the archaeo-

Table 1. Number of models out of 100 resolving parameters within tolerance (see text for details) for each scenario.

Parameter	Fault side	Scenario 1	Scenario 2	Scenario 3
Fault location (geometry)	–	11	15	23
Resistivity (middle layer)	Left	6	15	53
Resistivity (middle layer)	Right	5	42	53
Velocity (middle layer)	Left	8	10	44
Velocity (middle layer)	Right	6	38	44

logical site of *Les Fontaines Salées* (salty fountains) (47.447303° N, 3.777127° E). The site lies in the southern part of the sedimentary Paris Basin, near the contact between the Variscan granite basement of the Morvan Massif and the overlying Mesozoic sedimentary cover (Léger et al. 2025). The area is structurally complex, being affected by the regional Bazoches fault with north–south orientation and subsidiary east–west faults.

Léger et al. (2025) collected several collocated ERT and SRT profiles perpendicular to fault structures and inverted them individually, using smoothness-constrained inversion, to investigate the mechanisms controlling the natural degassing of helium (He) and hydrogen (H_2) along fault zones. In the present study, we focus on a profile originally referred to as L2, encompassing a granite/sediment contact across a normal fault, with sedimentary units expected on the west (left) side of the fault and granite to the east (right). This profile consists of collocated ERT and SRT data; however, the sensor positions were not identical along the profile, and the SRT profile covered only $\sim$50% of the ERT profile. The ERT data were collected using 96 electrodes with an in-line electrode spacing of 5 m, resulting in a 475 m long profile. It was acquired using dipole–dipole and Wenner–Schlumberger array configurations. The SRT survey is shorter and was carried out along the central portion of the ERT line using 120 geophones at regular distances of 1 m, with seismic shots every 2 m. Two roll-along deployments with 50% overlap resulted in a 240 m long profile. The results are presented only for the section where ERT and SRT profiles overlap, that is, at profile distances between 117 and 357 m.

Preliminary tests using our joint inversion approach outlined in Sec. 2.2.3, and conventional smoothness-constrained inversion results showed that at least four layers (three interfaces) at each side of the fault may be required to properly characterize the resistivity and seismic-velocity distribution at this site. However, when using our model parameterization considering only homogeneous layers, the resulting models were characterized by large data misfits, with ϕ_{ert} and ϕ_{srt} values typically exceeding 20%, and showing a significant diversity of model solutions. Therefore, we fixed the resistivity and velocity values in the heterogeneous upper $\sim$8 m (where alluvial, colluvial, or highly weathered materials are expected) to those obtained from the smoothness-constrained inversions. These near-surface values were mapped onto the meshes generated during the PSO inversion using spline interpolation. Fixing the near-surface model parameters allows the inversion to focus on the deeper subsurface structure, where the assumption of homogeneous layers is more appropriate. After this modification, the resulting inverted models generally achieved ϕ_{ert} and ϕ_{srt} values below 10%.

Preliminary tests inverting the field data using $w_{\mathrm{srt}} = 1/2$ (i.e. equal weights for the data misfit terms in Eq. 3) led to inversion results that were disproportionately influenced by the ERT data. To further investigate this imbalance, we evaluated three weighting schemes with $w_{\mathrm{srt}} = 1/2$, $2/3$, and $3/4$, corresponding to relative weights of the SRT and ERT misfit terms of 1:1, 2:1, and 3:1, respectively. In the end, we generated a total of 60 models, 20 for each weighting scheme.

Figs. 7a–b show the convergence histories of the individual misfit terms, ϕ_{srt} and ϕ_{ert}. Note that although the inversion minimizes the combined objective function rather than each term individually, plotting them separately illustrates how their convergences differ with the different weighting schemes. Fig. 7a shows the convergence of ϕ_{srt}, and Fig. 7b that of ϕ_{ert}. The insets in both panels summarize the distribution of misfit values at the final iteration (iteration 150), providing a clearer comparison of the final misfit levels obtained with each weighting scheme. With $w_{\mathrm{srt}} = 1/2$, the convergence of ϕ_{srt} takes longer, and their final misfit values remain noticeably higher than in the other cases. However, with $w_{\mathrm{srt}} = 2/3$ or $3/4$, more weight is given to the SRT misfit, yielding a steeper initial decrease and similar final misfit levels. The behavior is opposite for ϕ_{ert}. With $w_{\mathrm{srt}} = 1/2$, the ERT misfit decreases most rapidly and reaches the lowest final values. With larger values of w_{srt}, the influence of SRT becomes bigger, the ERT misfit decreases more slowly, and reaches larger final values. Overall, a weight-ratio $w_{\mathrm{srt}}/(1 - w_{\mathrm{srt}})$ of 2:1 (i.e. $w_{\mathrm{srt}} = 2/3$) seems to be a good compromise in the convergence behavior of the two data sets.

From the 20 models generated for each weighting scheme, we selected the two models with the lowest values of the objective function. These are shown in Figs. 8a-ℓ. This selection provides a concise set of representative solutions while avoiding redundancy and allowing a clearer comparison across weighting cases. Figs. 8a–f present the resistivity models, and Figs. 8g–ℓ the corresponding velocity models. Fig. 8a is the only model showing the fault slightly dipping to the left (west), while the remaining models depict a slight dip towards the right (east). These variations highlight the inherent ambiguity in the fault orientation, although all solutions consistently identify a discontinuity at profile distances between 275 and 300 m. Despite these differences, such results can provide valuable guidance for future exploration. For example, if borehole-based investigations were to be carried out, placing one borehole near 260 m and another around 310 m along the profile (on opposite sides of the inferred fault) would provide the most useful constraints for determining the vertical offset and

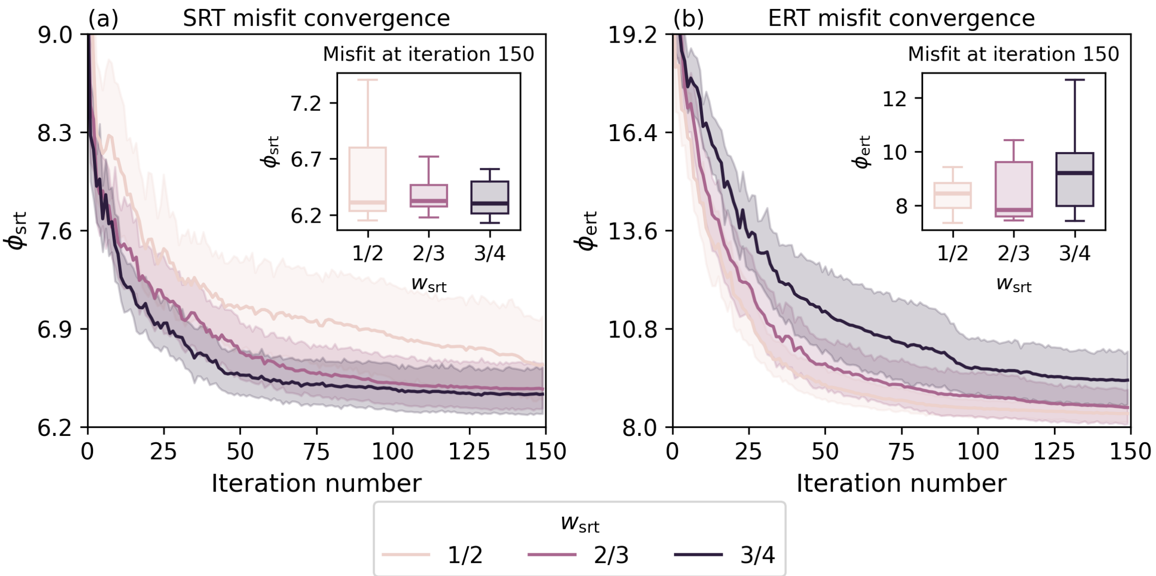

Figure 7. Convergence rates for the misfit terms in Eq. 3. Panel (a) shows the convergence of the ϕ_{srt} term, and panel (b) shows the convergence of ϕ_{ert}. Results are shown for the three cases with $w_{\mathrm{srt}} = 1/2, 2/3$, and $3/4$. The solid lines show the mean convergence behavior of the misfit terms, while the shaded regions represent the 95% confidence interval of the mean, computed from all the inversion runs for each w_{srt}. Each panel also includes an inset boxplot showing the distribution of the corresponding misfit at the final iteration (iteration 150). Note that although the two misfit terms (ϕ_{srt} and ϕ_{ert}) are shown separately, the objective function is a weighted sum of both.

refining the inversions. Interface depths obtained from these boreholes could be incorporated into the LBMP inversion to further constrain fault displacement and layer properties, as demonstrated in our synthetic example.

All models exhibit a consistent pattern of resistivity on the right (east) side of the fault, where resistivity generally increases with depth (Figs. 8a-f). In contrast, the left (west) side shows substantially greater variability among realizations, indicating that this portion of the model is less constrained. A recurring feature in several models (Figs. 8b, and d-f) is the presence of a low-resistivity layer (below 6 Ωm) on the left side of the fault at intermediate elevations (130-140 m), although its depth and thickness differ from model to model. The occurrence of this low-resistivity layer could indicate brine-saturated or clay-rich sediments according to the log provided in Léger et al. (2025). If confirmed by boreholes, it may serve as a useful low-resistivity marker horizon for regional correlation or for identifying additional faults. However, in this profile, the unit is only present on the left side of the fault, whereas the right side is characterized by much higher resistivities associated with granite. Therefore, it cannot be used here to estimate the fault offset, but it may be useful in other areas where the unit occurs on both sides of the fault.

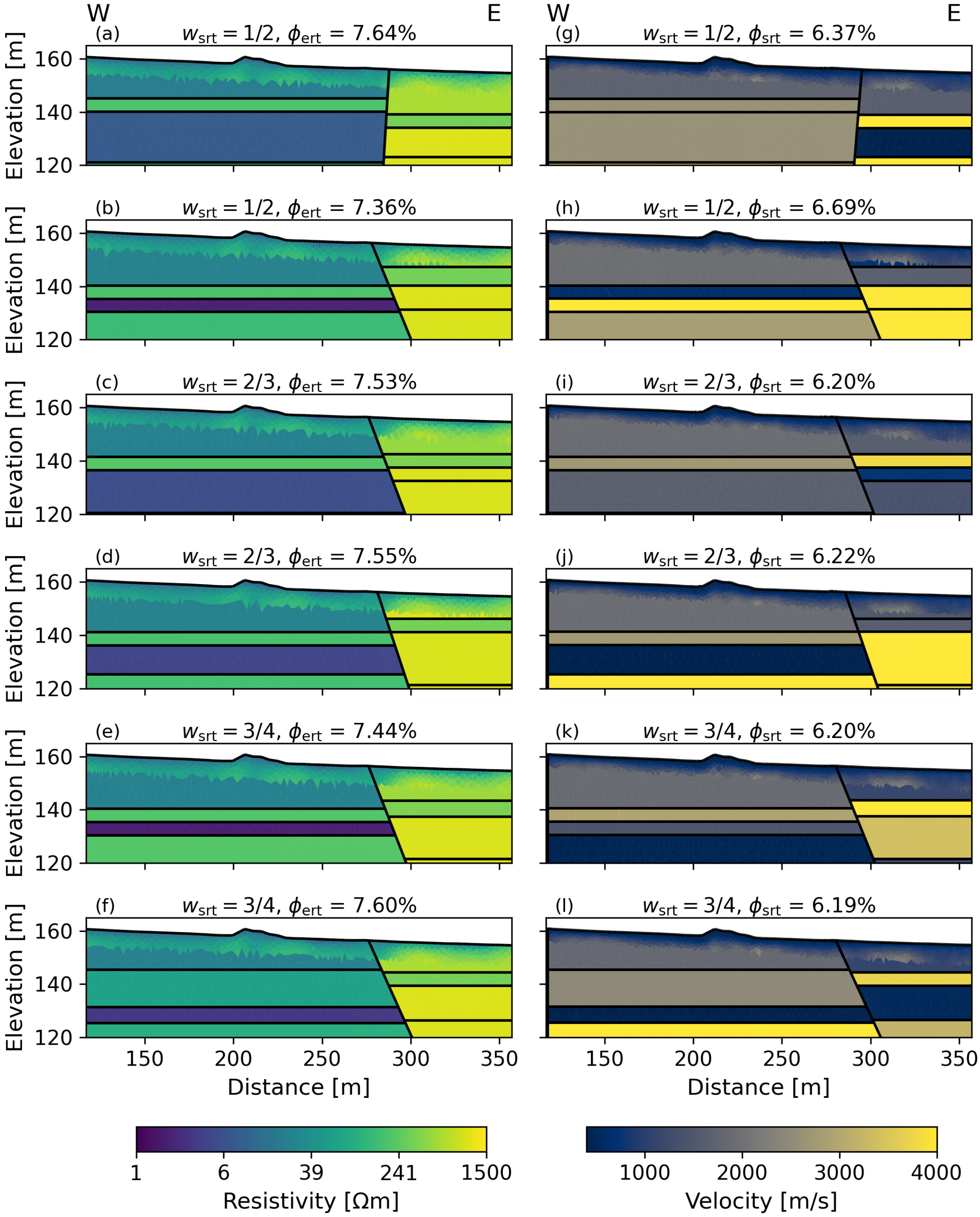

Figure 8. Joint inversion results for the ERT and SRT field data. For each weighting factor (w_{srt} = 1/2, 2/3, 3/4) in the objective function (Eq. 3), the two models with the lowest values of the objective function are shown. Panels (a–f) show the resulting resistivity models, and panels (g–ℓ) show the corresponding seismic velocity models. The values of ϕ_{ert}, ϕ_{srt}, and w_{srt} are indicated at the top of the respective panels. The labels W and E on top of panels (a) and (g) indicate the west and east directions, respectively.

The velocity models (Figs. 8g–ℓ) show a broadly consistent structure at elevations higher than $\sim$ 140 m on both sides of the fault, where velocities gradually increase from about 500 to 2000 m/s. On the right side, all realizations exhibit a pronounced velocity increase at an elevation of $\sim$ 140 m, marking a well-defined refractor beneath the shallow low-velocity units. This elevation also coincides with the sharp resistivity increase, indicating that both methods detect the same subsurface transition. A similar, though less sharply defined, velocity increase is detected on the left side at comparable depths. The different nature of this refractor across the fault suggests differing material properties on each side, a pattern that is also evident in the resistivity models. At elevations lower than $\sim$ 135 m, the models display increased variability in velocity, which most likely reflects the limited SRT sensitivity rather than a true low-velocity layer or refracting interface.

To further examine the variability in the inferred fault geometry, Fig. 9 shows boxplots of horizontal fault positions for the three weighting schemes, evaluated at 10 m elevation intervals between 110 and 150 m. At 150 m, the variability is slightly larger than at 140 m. This is expected because the model parameters within the shallowest 8 m were fixed. Thus, changes in fault position at elevations above 150 m are effectively insensitive and merely reflect the projection of the fault geometry inferred below the fixed portion of the model domain. The variability is approximately 10 m at an elevation of 140 m and increases to nearly 80 m at an elevation of 110 m. This increased variability at lower elevations is consistent with the reduced sensitivity of the ERT and SRT data. Note that if we connect the median values (central lines of the boxplots) across elevations, they indicate the trace of a steeply dipping normal fault. Furthermore, connecting other percentile values across elevations indicates that both left- and right-dipping fault geometries are common. This implies that the six best models shown in Fig. 8 underrepresent the range of plausible solutions, highlighting the importance of considering other visualization strategies for assessing and understanding uncertainties.

We used the smoothness-constrained geometry-preserving inversion approach outlined in Sec. 2.2.4 to evaluate whether this additional inversion step could introduce meaningful refinements beyond the LBMP results. The corresponding results of this test are shown in Fig. 10. To obtain these results, the resistivity and velocity models shown in Fig. 8 were used as both the starting and reference models. The corresponding geometry (that is, the interfaces of layers and the fault line) was explicitly incorporated as structural constraints by eliminating smoothing across the interfaces (i.e., diagonal elements of $\mathbf{W}_\mathrm{c}$ were set to zero for boundaries separating two different zones), thereby preserving sharp parameter contrasts between the layers and across the fault line. The regularization parameter in Eq. 6 was set to 20 (after some preliminary tests). The smoothness-constrained models achieved substantially lower misfits (where ϕ_ert ranges from 1.85% to 2.08%, and ϕ_srt from 2.31% to 2.61%) than their corresponding LBMP starting models (ϕ_ert ranging from 7.36% to 7.64% and ϕ_srt from 6.19% to

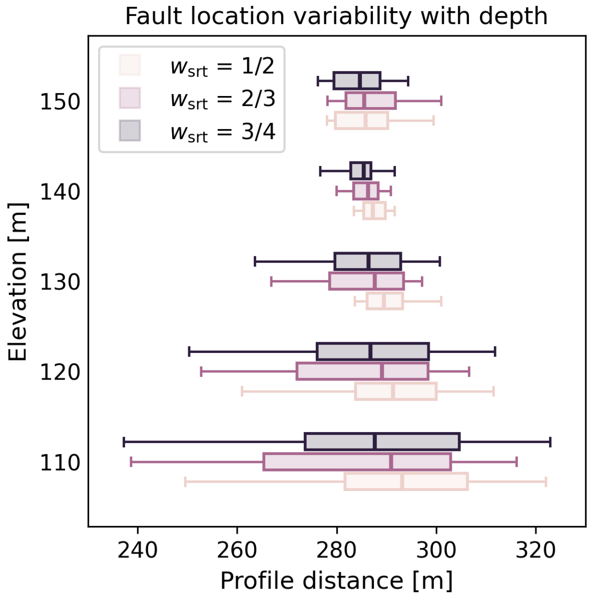

Figure 9. Estimated fault position at different depths for the three cases with $w_{srt} = 1/2, 2/3$, and $3/4$. Boxplots show the distribution of lateral fault locations derived from all obtained inversion models at 10 m elevation intervals. The spread of each distribution reflects the depth-dependent uncertainty in the inferred fault position.

6.69%). Despite the reduced misfits, the recovered structural features remain essentially unchanged, showing only minor adjustments within the layers. This outcome shows that, despite yielding higher misfits, the LBMP joint-inversion models recover the same underlying structure as the admissible solutions from the smoothness-constrained inversion. This implies that our joint inversion strategy using an LBMP approach, with a reduced number of model parameters, is still able to capture essential structural elements and eases the direct interpretation of sharp boundaries, including faults.

4 DISCUSSION

4.1 Challenges and Opportunities in Near-Surface Fault Characterization

Identifying faults in the near subsurface is challenging for several reasons. Alluvial and colluvial deposits may bury the fault zone so that faulted units are only encountered at depth, while weathering can reduce the resistivity and velocity contrasts typically associated with fault structures. Even when stronger contrasts are present at depth, the sensitivity of ERT and SRT naturally decreases with depth, which limits the precision by which fault geometries can be resolved. This reduced sensitivity, combined with compensatory trade-offs among parameters such as layer thickness, resistivity, and velocity, causes multiple model configurations explaining the data equally well. In this situation, presenting a

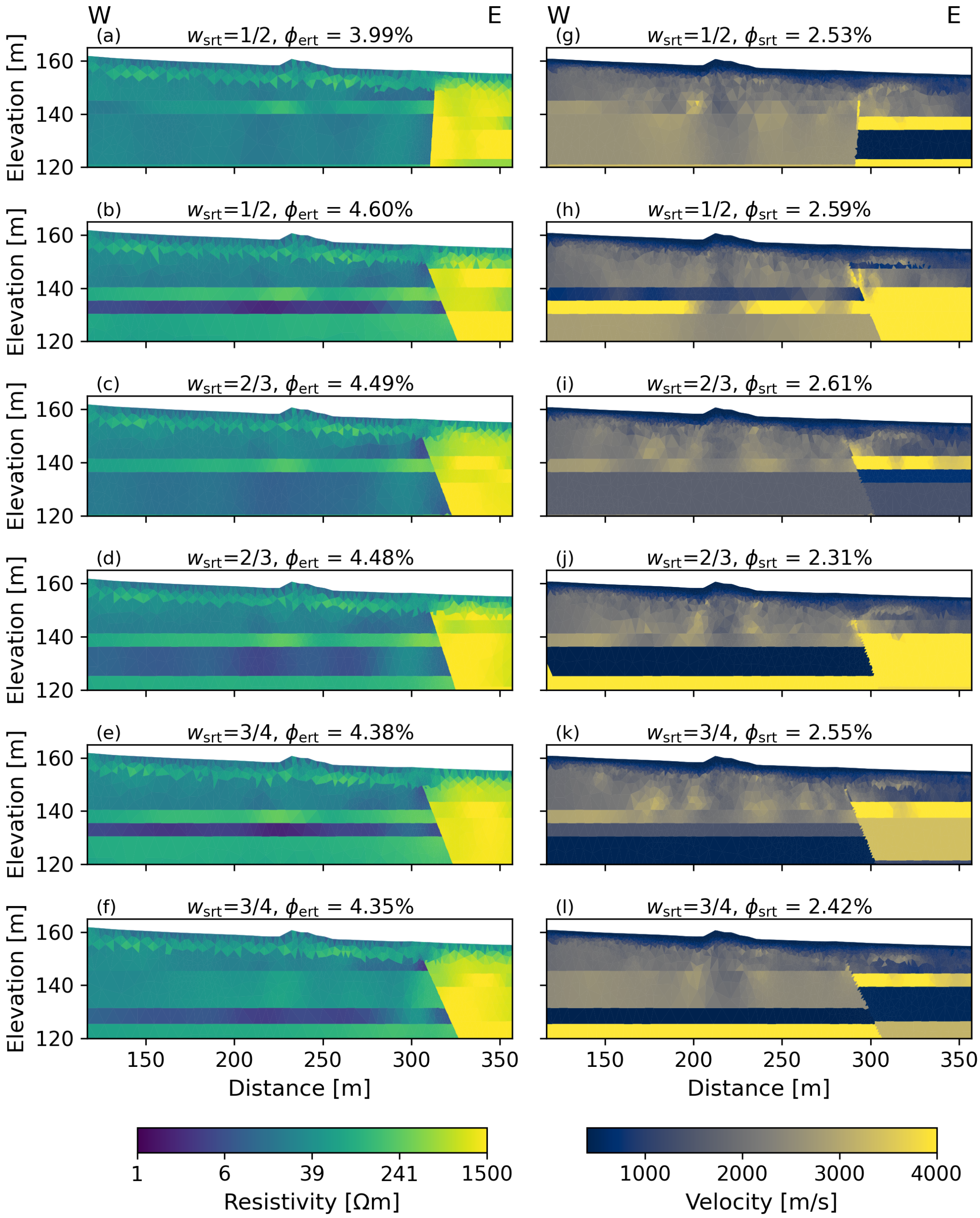

Figure 10. Smoothness-constrained geometry-preserving inversion results obtained using the layered models presented in Fig. 8 as both starting and reference models. Panels (a–f) show the resulting resistivity models, and panels (g–l) display the corresponding seismic velocity models. The values of ϕ_{ert} and ϕ_{srt}, and w_{srt} are indicated at the top of the respective panels. The labels W and E on top of panels (a) and (g) indicate the west and east directions, respectively.

range of plausible model solutions becomes a transparent way of communicating the uncertainty of the results –as illustrated in this study.

Our synthetic and field examples demonstrate that generating multiple solutions through the joint inversion of ERT and SRT data provides deeper insights into the subsurface structure than relying on either method alone or on a single inversion result. Because the two methods are sensitive to different physical properties, each constrains different aspects of the structure. Features that are weakly expressed in one method may be more clearly resolved in the other. This complementary behavior is reflected in our joint inversion results, where some inversion runs converged to velocity and resistivity models with different numbers of layers. Such differences likely arise from how model parameters evolve during the optimization, particularly given the diverse set of randomly generated starting models. Such differences among resistivity and velocity models indicate that interpretations based solely on a single dataset, or on a single inversion, may be biased (e.g., two- vs. three-layer models). Analyzing ensembles of model solutions might help identifying which structural features are consistently resolved and which ones remain ambiguous, thereby providing a more transparent and quantitative picture of alternative subsurface scenarios.

Having multiple solutions was also relevant for investigating how well we can identify a fault structure. The results from the investigated data sets show that the approximate fault position is consistent across model solutions, suggesting that when a fault produces a sufficiently strong lateral contrast in physical properties, its location can typically be resolved with an accuracy of a few meters in the near subsurface, decreasing to tens of meters at depth. However, the fact that both normal- and reverse-fault geometries, as well as a range of vertical offsets, yield comparable data misfits underscores the remaining non-uniqueness of the inversion. This ambiguity has direct implications for applications where a fault governs subsurface flow or containment (for example, aquifer connectivity and fluid migration). In such contexts, resolving the geometry and internal properties of the fault zone requires complementary information such as borehole observations, cross-borehole geophysics, and targeted hydraulic or tracer tests, which can provide the additional constraints needed to reliably characterize the fault zone (e.g., Roques et al. 2014; Sproule et al. 2021; Boura et al. 2024; Balza-Morales et al. 2025).

One practical way to incorporate additional constraints is through geological information obtained from strategically placed boreholes. In this regard, joint inversion results can help guide the optimal placement of boreholes to reduce uncertainty. For example, in our synthetic example (Sec. 3.1), we first assumed borehole information on the right side of the fault and then added a borehole on the left side. As expected, the most informative results were obtained when boreholes were positioned on both sides of the expected fault location. This experiment shows how incorporating additional constraints iteratively improves estimates of the structure and physical parameters that more closely match the truth. In real-case scenarios, such boreholes should be located far enough from the fault to avoid strongly perturbed formations (which may make geological interpretations difficult), yet close enough to meaningfully constrain the geometry and avoid alternative interpretations such as folding or dipping layers (e.g., Wellmann et al. 2010). Another type of constraint that can be readily incorporated is the expected fault type and the dip angle, provided such information is available. For example, if prior geological knowledge indicates a normal fault, the inversion can be configured to penalize model updates that produce reverse-fault geometries, thereby guiding the optimization toward solutions consistent with the expected fault type. Overall, our findings underscore both the value of prior information and the need to interpret inverted models cautiously.

In addition to geological constraints, an important consideration in joint inversion is the relative weighting of the ERT and SRT misfit terms in the objective function (see Eq. 3), as unbalanced weights can cause the inversion to converge toward a local minimum dominated by one dataset. This behavior is evident in our field example, where equal weights (i.e. $w_{\text{srt}} = 1/2$) led to a dominant influence of the ERT data, likely reflecting differences in the sensitivity of the two methods to the physical properties at the site. Adjusting the relative weights improved the balance between datasets and likely helped avoiding structurally biased results. In this context, convergence histories were particularly informative for diagnosing such imbalances. For example, rapid early convergence of one misfit term indicates that this dataset may act as the structural guide ("starting model") for the other dataset with a slower convergence rate. This underscores the importance of well-informed initial models, as a realistic starting structure helps preventing the inversion falling prematurely toward solutions dominated by a single data set and may increase the likelihood of converging to plausible geological models. As an alternative way to prevent structural dominance by a single dataset, one could relax the structural similarity constraint by allowing ERT and SRT to use different structural models while adding a penalty term to discourage large geometric discrepancies; this would explicitly test whether the two methods support a consistent subsurface structure.

Besides inversion choices and constraints, the effectiveness of joint inversion of ERT and SRT data for fault characterization also relies on the particularities of the field site. For example, having distinct geological units that exhibit relatively high resistivity or velocity contrasts across the fault will increase the likelihood of better resolving the fault zone and its geometry. In our field example (Fig. 8), several realizations reveal a layer with very low resistivity that is distinct from the overlying and underlying units. If the presence of such a low-resistivity unit is confirmed, it may serve as a regionally traceable resistivity marker for estimating vertical fault offsets at different locations in the region. However, along our studied ERT profile, this sedimentary unit is present only on the left (west) side of the fault, while granite occurs on the right (east) side, preventing its use for offset estimation. Finally, any model adjustments made after inversion (for example, manual refinements informed by geological reasoning) should be verified by re-evaluating the data residuals. If the modification of the model parameters results in a large increase in data misfit, it is likely inconsistent with the observations; however, if the changes reduce or only slightly increase the misfit, the adjusted structure may still represent a valid solution of the inverse problem.

4.2 Feasibility and Methodological Opportunities for Joint Inversion

The proposed LBMP proved effective in both synthetic and field applications in several key aspects. First, the parameterization relies on a limited set of model parameters describing horizontally continuous, homogeneous layers offset by a single fault line. This is particularly advantageous for global-search methods such as PSO, which benefit from a reduced parameter space and are less prone to premature convergence into a local minimum with high misfits. Second, the approach is flexible with respect to assumptions about physical properties. For example, traditional smoothness-constrained inversion approaches of seismic data often impose a monotonic increase of velocity with depth, whereas relaxing this constraint within the LBMP framework allows the inversion to recover alternative models that may better reflect the complexity of the near subsurface (e.g., low velocity layers at intermediate depths). Third, the method can be adapted to practical field conditions: the joint inversion does not require coincident ERT and SRT layouts. Our field example demonstrates that reliable results can still be obtained when sensor distributions differ, which is valuable in surveys where identical acquisition geometries are impractical. However, when operationally feasible, collecting coincident ERT and SRT measurements remains preferable because it reduces preprocessing steps and allows inverting both data sets using a common computational mesh.

Despite the strengths outlined above, the field application also revealed important limitations that are worth considering in practice. For example, in preliminary tests, when we used our joint inversion approach to invert the field data considering only homogeneous layers, it failed to achieve acceptable data misfits. Such large misfits reflect heterogeneity within the zones of materials identified by our LBMP approach. Because deterministic smoothness-constrained inversions generally resolve the shallow subsurface reliably (both using ERT and SRT surveys), we adopted a hybrid strategy in which the resistivity and velocity in the shallowest layer were fixed to the values obtained from the smooth inversions. This allowed the joint inversion to focus on updating the deeper structure, where the assumption of homogeneous layers is more appropriate, which substantially improved the overall data misfit. While effective, this procedure inevitably introduces a degree of decision-making by the user regarding how much near-surface information should be incorporated from deterministic inversions.

A second complementary strategy was explored to evaluate whether the data misfit in the field example could be reduced by allowing changes in the model parameters (resistivities and velocities) within each layer in our models obtained using our LBMP inversion. This was achieved by using the layered models as both starting and reference models and by removing the regularization coupling across layer interfaces and the fault (that is, setting the corresponding entries of $\mathbf{W}_c$ to zero for boundaries separating distinct zones) in subsequent smoothness-constrained inversions. Decoupling cells across sharp boundaries helps preserving the original structural geometry and allows for sharp variations in model parameters (e.g., Bergmann et al. 2014; Wunderlich et al. 2018). Additionally, it is important to note that the regularization parameter λ (see Eq. 6) plays a key role in the inversion and strongly influences the similarity of the resulting model to the starting and reference models. Therefore, it is advisable to perform several inversion runs considering different values of λ to assess its overall impact on the resulting model. Overall, this two-step approach proved effective in lowering the data misfits, as the deterministic inversion introduced minor lateral and vertical adjustments within the layers. An additional extension would be to incorporate image-guided regularization (e.g., Zhou et al. 2014), in which structural information extracted from the layered models directly informs the deterministic inversion.

We emphasize that the simplified parameterization strategy presented here can be adapted to allow for more complex structural features. For example, interfaces may be parameterized using functions that can represent folding or tilting, such as sums of arctangent functions, polynomial functions, or splines (e.g., Arboleda-Zapata et al. 2022b; Koren et al. 1991). Additionally, instead of representing the fault as a single line, it could be modeled as a finite-width buffer zone that captures fractured and/or mineralized materials typically associated with fault cores and damage zones. Similarly, the assumption of homogeneous layers can be relaxed by introducing lateral variations (e.g., by using spline functions or geostatistical descriptors) that are estimated simultaneously with the interface geometry during a single inversion run. With this approach, we can avoid the two-step inversion procedure used in our field example and may be particularly relevant at sites where lateral facies transitions or near-surface heterogeneity are significant.

The primary limitation of the proposed workflow is its computational cost, which can increase further when greater geometric flexibility is allowed, since the latter requires additional model parameters and, consequently, more particles and iterations in PSO. Typically, several thousand forward simulations may be required to explore the solution space adequately. For example, one inversion run of our field data takes about 20 hours on a single core of a modern desktop computer. However, this effort is justified by the improved understanding of the structure as well as the variability and trade-offs among the model parameters; insights that are essential for subsequent analyses requiring well-constrained structural features (e.g., Arboleda-Zapata et al. 2022a; Zhou et al. 2014). A promising avenue to further accelerate the LBMP approach is to train machine-learning surrogate models that emulate forward responses (e.g., Aleardi et al. 2022), thereby substantially reducing computation time while preserving the ability to explore nonlinear parameter interactions. It is also important to highlight that the proposed workflow is general and can be readily adapted to jointly invert other types of geophysical datasets beyond ERT and SRT (e.g., electromagnetic and gravity data). It can also accommodate objective functions with more than two misfit terms, enabling the integration of additional collocated observations or the inclusion of penalty terms that suppress undesired structural features. Furthermore, the workflow is not restricted to PSO and can be combined with other global or hybrid inversion strategies.

5 CONCLUSIONS

This study introduced a joint inversion workflow for ERT and SRT data based on a layer-based model parameterization that relies on a reduced number of model parameters to represent layers and faults. Such a parameterization is well-suited for global optimization algorithms like PSO, as it constrains the search space, allowing the exploration of multiple subsurface scenarios in an efficient and interpretable way. When expecting sharp structural boundaries, our parameterization approach offers a clear advantage over inversion approaches relying on pixel-based updates, which typically result in smoothed models. Additionally, because our inversion workflow incorporates randomized starting models and the intrinsic stochasticity of PSO, it is possible to obtain an ensemble of plausible model solutions. Such an ensemble can be used to identify which features are consistently resolved across solutions and which remain uncertain, making the workflow an explicitly uncertainty-aware approach.

A further advantage of the workflow is its flexibility. It accommodates non-coincident ERT–SRT layouts, relaxes common assumptions such as monotonic increases in seismic velocity, and can be combined with smoothness-constrained deterministic inversions. In the latter case, the resulting sharp models provide the primary structural framework while deterministic inversion refines lateral variability within layers and improves data fit. More broadly, these features illustrate that the workflow can be adapted to a range of practical field conditions and integrated with complementary inversion strategies, making it suitable for applications that require both sharp structural delineation and internal heterogeneity.

Joint inversion using the proposed parameterization consistently constrains the fault location to within a few meters; however, substantial non-uniqueness remains even with a reduced number of model parameters. Different layer configurations, vertical offsets, and even opposite fault dips can fit the data to comparable levels, highlighting the importance of incorporating independent geological constraints. Information such as interface depths from boreholes or the expected fault type and dip direction can substantially reduce ambiguity and can be readily integrated into the parameterization and inversion framework. Although this study focuses on relatively simple geological settings, the parameterization is easily extendable to more complex structural features, including multiple faults, finite-width fault zones, and laterally varying layer properties. Overall, the proposed workflow provides a practical and uncertainty-aware approach for near-surface fault detection, providing valuable guidance for follow-up investigations such as borehole placement and targeted geophysical surveys.

6 ACKNOWLEDGMENTS

This work was funded by the Deutsche Forschungsgemeinschaft (DFG) under project numbers CI 26/19-1, DI 833/25-1, and LE 2398/3-1.

7 DATA AVAILABILITY STATEMENT

The field ERT and SRT data sets used in this paper are published by Léger et al. (2025). The corresponding scripts will be made publicly available upon acceptance of the manuscript.

REFERENCES

Abril, J. L., Vasconcelos, M. A., Barboza, F. M., & Mojica, O. F., 2022. A parallel improved PSO algorithm with genetic operators for 2D inversion of resistivity data, *Acta Geophysica*, **70**, 1137–1154.

Aleardi, M., Vinciguerra, A., Stucchi, E., & Hojat, A., 2022. Probabilistic inversions of electrical resistivity tomography data with a machine learning-based forward operator, *Geophysical Prospecting*, **70**(5), 938–957.

Alt-Epping, P., Diamond, L. W., Wanner, C., & Hammond, G. E., 2021. Effect of Glacial/Interglacial Recharge Conditions on Flow of Meteoric Water Through Deep Orogenic Faults: Insights Into the Geothermal System at Grimsel Pass, Switzerland, *Journal of Geophysical Research: Solid Earth*, **126**(7).

Arboleda-Zapata, M., Angelopoulos, M., Overduin, P. P., Grosse, G., Jones, B. M., & Tronicke, J., 2022a. Exploring the capabilities of electrical resistivity tomography to study subsea permafrost, *The Cryosphere*, **16**(10), 4423–4445.

Arboleda-Zapata, M., Guillemoteau, J., & Tronicke, J., 2022b. A comprehensive workflow to analyze ensembles of globally inverted 2D electrical resistivity models, *Journal of Applied Geophysics*, **196**, 104512.

Arboleda-Zapata, M., Leven, C., Drach, K., Dietrich, P., & Cirpka, O., 2025a. A Targeted Approach for Imaging Near-Surface Geological Faults using Geophysical Surveying, in *NSG 2025: 31st Meeting of Environmental and Engineering Geophysics*, pp. 1–5, European Association of Geoscientists & Engineers, Naples.

Arboleda-Zapata, M., Osterman, G., Li, X., Sasidharan, S., Dahlke, H. E., & Bradford, S. A., 2025b. Time-lapse ensemble-based electrical resistivity tomography to monitor water flow from managed aquifer recharge operations, *Journal of Hydrology*, **659**, 133282.

Arnous, A., Zeckra, M., Venerdini, A., Alvarado, P., Arrowsmith, R., Guillemoteau, J., Landgraf, A., Gutiérrez, A., & Strecker, M. R., 2020. Neotectonic Activity in the Low-Strain Broken Foreland (Santa Bárbara System) of the North-Western Argentinean Andes (26_S), *Lithosphere*, **2020**(1), 1–25.

Audin, L., Lacan, P., Tavera, H., & Bondoux, F., 2008. Upper plate deformation and seismic barrier in front of Nazca subduction zone: The Chololo Fault System and active tectonics along the Coastal Cordillera, southern Peru, *Tectonophysics*, **459**(1-4), 174–185.

Bailly, C., Fortin, J., Adelinet, M., & Hamon, Y., 2019. Upscaling of Elastic Properties in Carbonates: A Modeling Approach Based on a Multiscale Geophysical Data Set, *Journal of Geophysical Research: Solid Earth*, **124**(12), 13021–13038.

Ball, L. B., Ge, S., Caine, J. S., Revil, A., & Jardani, A., 2010. Constraining fault-zone hydrogeology through integrated hydrological and geoelectrical analysis, *Hydrogeology Journal*, **18**(5), 1057–1067.

Balza-Morales, A., Grab, M., Rinaldi, A. P., Zappone, A., Maurer, H., & Wagner, F. M., 2025. Electrical resistivity monitoring of CO2 injection at the Mont Terri underground laboratory, Switzerland, *Journal of Applied Geophysics*, **242**.

Bardot, K., Grose, L., Camargo, I., Pirot, G., Siade, A., Pigois, J. P., Hampton, C., & McCallum, J., 2025. A seamless geo-flow modelling workflow to tackle structural uncertainty using LoopStructural and MODFLOW, *Environmental Modelling and Software*, **192**.

Barnes, H., Hinojosa, J. R., Spinelli, G. A., Mozley, P. S., Koning, D., Sproule, T. G., & Wilson, J. L., 2021. Detecting fault zone characteristics and paleovalley incision using electrical resistivity: Loma Blanca Fault, New Mexico, *Geophysics*, **86**(3), B209–B221.

Bense, V., Gleeson, T., Loveless, S., Bour, O., & Scibek, J., 2013. Fault zone hydrogeology, *Earth-Science Reviews*, **127**, 171–192.

Bense, V. F. & Person, M. A., 2006. Faults as conduit-barrier systems to fluid flow in siliciclastic sedimentary aquifers, *Water Resources Research*, **42**(5).

Bergmann, P., Ivandic, M., Norden, B., Rücker, C., Kiessling, D., Lüth, S., Schmidt-Hattenberger, C., & Juhlin, C., 2014. Case history: Combination of seismic reflection and constrained resistivity inversion with an application to 4D imaging of the CO2 storage site, Ketzin, Germany, *Geophysics*, **79**(2), B37–B50.

Bezerra-Guedes, V. J. C., Ramalho-Maciel, S. T., & Peres-Rocha, M., 2022. Refrapy: A Python program for seismic refraction data analysis, *Computers & Geosciences*, **159**, 105020.

Binley, A. & Slater, L., 2020. *Resistivity and induced polarization*, Cambridge University Press.

Bloom, C. K., Howell, A., Stahl, T., Massey, C., & Singeisen, C., 2022. The influence of off-fault deformation zones on the near-fault distribution of coseismic landslides, *Geology*, **50**(3), 272–277.

Boura, A., Cousquer, Y., Clauzon, V., Valois, R., & Leonardi, V., 2024. Improving Fault Zones Hydrodynamic Characterization and Simulation in Karstified Carbonate Environments with GLM and IES Invers Methods, *Journal of Hydrology*, **645**.

Caputo, R., Salviulo, L., Piscitelli, S., & Loperte, A., 2007. Late Quaternary activity along the Scorciabuoi Fault (Southern Italy) as inferred from electrical resistivity tomographies, *Annals of Geophysics*, **50**(2).

Carreón-Freyre, D., Cerca, M., Ochoa-González, G., Teatini, P., & Zuñiga, F. R., 2016. Shearing along faults and stratigraphic joints controlled by land subsidence in the Valley of Queretaro, Mexico, *Hydrogeology Journal*, **24**(3), 657–674.

Chen, H. & Niu, Q., 2022. Improving moisture content estimation from field resistivity measurements with subsurface structure information, *Journal of Hydrology*, **613**.

Chen, J. & Zelt, C. A., 2016. Application of Frequency-dependent Traveltime Tomography and Full Waveform Inversion to Realistic Near-surface Seismic Refraction Data, *Journal of Environmental and Engineering Geophysics*, **21**(1), 1–12.

Clair, J. S., Moon, S., Holbrook, W. S., Perron, J. T., Riebe, C. S., Martel, S. J., Carr, B., Harman, C., Singha, K., De Richter, D. B., St Clair, J., Moon, S., Holbrook, W. S., Perron, J. T., Riebe, C. S., Martel, S. J., Carr, B., Harman, C., Singha, K., deB Richter, D., Clair, J. S., Moon, S., Holbrook, W. S., Perron, J. T., Riebe, C. S., Martel, S. J., Carr, B., Harman, C., Singha, K., & De Richter, D. B., 2015. Geophysical imaging reveals topographic stress control of bedrock weathering, *Science*, **350**(6260), 534–538.

Comte, J. C., Cassidy, R., Nitsche, J., Ofterdinger, U., Pilatova, K., & Flynn, R., 2012. The typology of Irish hard-rock aquifers based on an integrated hydrogeological and geophysical approach, *Hydrogeology Journal*, **20**(8), 1569–1588.

Díaz, D., Maksymowicz, A., Vargas, G., Vera, E., Contreras-Reyes, E., & Rebolledo, S., 2014. Exploring the shallow structure of the San Ramón thrust fault in Santiago, Chile (33.5° S), using active seismic and electric methods, *Solid Earth*, **5**(2), 837–849.

Drahor, M. G. & Berge, M. A., 2017. Integrated geophysical investigations in a fault zone located on southwestern part of İzmir city, Western Anatolia, Turkey, *Journal of Applied Geophysics*, **136**, 114–133.

D'Affonseca, F. M., Finkel, M., & Cirpka, O. A., 2020. Combining implicit geological modeling, field surveys, and hydrogeological modeling to describe groundwater flow in a karst aquifer, *Hydrogeology Journal*, **28**(8), 2779–2802.

Fadili, A., Boualla, O., Najib, S., Makan, A., Mehdi, K., Bouzerda, M., Bouftou, H., Mehdi, I., Kharis, A. A., Achnouni, M., Belkaid, B., & Zourarah, B., 2024. Geophysical investigation of structural involvement in collapse dolines belong Abda region, western Morocco, *Acta Geophysica*.

Fazzito, S. Y., Rapalini, A. E., Cortés, J. M., & Terrizzano, C. M., 2009. Characterization of Quaternary faults by electric resistivity tomography in the Andean Precordillera of Western Argentina, *Journal of South American Earth Sciences*, **28**(3), 217–228.

Fischer, P., Wunderlich, T., Rabbel, W., Vött, A., Willershäuser, T., Baika, K., Rigakou, D., & Metallinou, G., 2016. Combined Electrical Resistivity Tomography (ERT), Direct-Push Electrical Conductivity (DP-EC) Logging and Coring – A New Methodological Approach in Geoarchaeological Research, *Archaeological Prospection*, **23**(3), 213–228.

Furman, A., Ferre, T. P. A., & Warrick, A. W., 2003. A sensitivity analysis of electrical resistivity tomography array types using analytical element modeling, *Vadose Zone Journal*, **2**(3), 416–423.

Galli, P. A. C., Giocoli, A., Peronace, E., Piscitelli, S., Quadrio, B., & Bellanova, J., 2014. Integrated near surface geophysics across the active Mount Marzano Fault System (southern Italy): seismogenic hints, *International Journal of Earth Sciences*, **103**(1), 315–325.

Ganerød, G. V., Rønning, J. S., Dalsegg, E., Elvebakk, H., Holmøy, K., Nilsen, B., & Braathen, A., 2006. Comparison of geophysical methods for sub-surface mapping of faults and fracture zones in a section of the Viggja road tunnel, Norway, *Bulletin of Engineering Geology and the Environment*, **65**(3), 231–243.

Gao, K. & Wellmann, F., 2025. Fault representation in structural modelling with implicit neural representations, *Computers & Geosciences*, **199**, 105911.

Giao, P. H., Weller, A., Hien, D. H., & Adisornsupawat, K., 2008. An approach to construct the weathering profile in a hilly granitic terrain based on electrical imaging, *Journal of Applied Geophysics*, **65**, 30–38.

Giraud, J., Caumon, G., Grose, L., Ogarko, V., & Cupillard, P., 2024. Integration of automatic implicit geological modelling in deterministic geophysical inversion, *Solid Earth*, **15**(1), 63–89.

Gómez-Vasconcelos, M. G., Avellán, D. R., García, J. A., Lacan, P., Israde-Alcántara, I., García, O., Castellano, J. A., & Audin, L., 2025. The potential seismic hazard of the Tarímbaro-Álvaro Obregón fault, a major structure of the Morelia-Acambay fault system in central México, *Natural Hazards*, **121**(1), 109–133.

Gonzalez-Duque, D., Gomez-Velez, J. D., Person, M. A., Kelley, S., Key, K., & Lucero, D., 2024. Groundwater Circulation Within the Mountain Block: Combining Flow and Transport Models With Magnetotelluric Observations to Untangle Its Nested Nature, *Water Resources Research*, **60**(4).

Hellman, K., Ronczka, M., Günther, T., Wennermark, M., Rücker, C., & Dahlin, T., 2017. Structurally coupled inversion of ERT and refraction seismic data combined with cluster-based model integration, *Journal of Applied Geophysics*, **143**, 169–181.

Hess, S., Fairley, J. P., Bradford, J., Lyle, M., & Clement, W., 2009. Evidence for composite hydraulic architecture in an active fault system based on 3D seismic reflection, time-domain electromagnetics and temperature data, *Near Surface Geophysics*, **7**(5-6), 341–352.

Jiang, C., Igel, J., Dlugosch, R., Müller-Petke, M., Günther, T., Helms, J., Lang, J., & Winsemann, J., 2020. Magnetic resonance tomography constrained by ground-penetrating radar for improved hydrogeophysical characterization, *Geophysics*, **85**(6), JM13–JM26.

Jiang, F., Dong, L., & Dai, Q., 2018. Electrical resistivity imaging inversion: An ISFLA trained kernel principal component wavelet neural network approach, *Neural Networks*, **104**, 114–123.

Jordi, C., Doetsch, J., Günther, T., Schmelzbach, C., Maurer, H., & Robertsson, J. O., 2020. Structural joint inversion on irregular meshes, *Geophysical Journal International*, **220**(3), 1995–2008.

Kennedy, J. & Eberhart, R., 1995. Particle swarm optimization, in *Proceedings of ICNN'95 - International Conference on Neural Networks*, vol. 4, pp. 1942–1948, IEEE.

Kong, S., Oh, J., Yoon, D., Ryu, D.-W., & Kwon, H.-S., 2023. Integrating Deep Learning and Deterministic Inversion for Enhancing Fault Detection in Electrical Resistivity Surveys, *Applied Sciences*, **13**(10), 6250.

Koren, Z., Mosegaard, K., Landa, E., Thore, P., & Tarantola, A., 1991. Monte Carlo estimation and resolution analysis of seismic background velocities.

Kruszewski, M., Montegrossi, G., Balcewicz, M., de Los Angeles Gonzalez de Lucio, G., Igbokwe, O. A., Backers, T., & Saenger, E. H., 2022. 3D in situ stress state modelling and fault reactivation risk exemplified in the Ruhr region (Germany), *Geomechanics for Energy and the Environment*, **32**, 100386.

Léger, E., Sarda, P., Bailly, C., Zeyen, H., Pessel, M., Portier, E., Dupuy, G., Lambert, R., Courtin, A., Guinoiseau, D., Calmels, D., Durand, V., Monvoisin, G., Battani, A., Moreira, M., Stuart, F., Barbarand, J., & Brigaud, B., 2025. Deciphering degassing mechanisms of He and H2 at the sedimentary basin-basement interface by surface geophysics and gas geochemistry, *Geochemistry, Geophysics, Geosystems*, **26**(4).

León-Loya, R., Lacan, P., Ortuño, M., Zúñiga, F. R., Štěpančíková, P., Stemberk, J., Hernández Flores, A. P., Carrera Hernández, J. J., Sunyé-Puchol, I., Aguirre-Díaz, G. J., & Audin, L., 2023. Paleoseismology of a Major Crustal Seismogenic Source Near Mexico City: The Southern Border of the Acambay Graben, *Tectonics*, **42**(6).

Lesparre, N., Boyle, A., Grychtol, B., Cabrera, J., Marteau, J., & Adler, A., 2016. Electrical resistivity imaging in transmission between surface and underground tunnel for fault characterization, *Journal of Applied Geophysics*, **128**, 163–178.

Lübben, A. & Leven, C., 2018. The Starzach site in Southern Germany: a site with naturally occurring CO2 emissions recovering from century-long gas mining as a natural analog for a leaking CCS reservoir, *Environmental Earth Sciences*, **77**(8), 316.

Malehmir, A., Andersson, M., Mehta, S., Brodic, B., Munier, R., Place, J., Maries, G., Smith, C., Kamm, J., Bastani, M., Mikko, H., & Lund, B., 2016. Post-glacial reactivation of the Bollnäs fault, central Sweden - A multidisciplinary geophysical investigation, *Solid Earth*, **7**(2), 509–527.

Menzel, N., Klitzsch, N., Altenbockum, M., Müller, L., & Wagner, F. M., 2024. Prospection of faults on the Southern Erftscholle (Germany) with individually and jointly inverted refraction seismics and electrical resistivity tomography, *Journal of Applied Geophysics*, **231**, 105549.

Miocic, J. M., Gilfillan, S. M., Frank, N., Schroeder-Ritzrau, A., Burnside, N. M., & Haszeldine, R. S., 2019a. 420,000 year assessment of fault leakage rates shows geological carbon storage is secure, *Scientific Reports*, **9**(1).

Miocic, J. M., Johnson, G., & Bond, C. E., 2019b. Uncertainty in fault seal parameters: Implications for CO2 column height retention and storage capacity in geological CO2 storage projects, *Solid Earth*, **10**(3), 951–967.

Moreira, C. A., Netto, L. G., de Freitas Schorcht, S., de Souza, I. A., Masquelin, H., Hansen, M. A. F., & Lima, J. P. R., 2025. Characterization of groundwater flow in the cuesta reverse from structural analysis and electrical resistivity tomography, *Discover Geoscience*, **3**(1).

Naik, S. P., Gwon, O., Park, K., Bae, S. Y., Shin, H.-C., Choi, J.-H., & Kim, Y.-S., 2022. Localization and characterization of the southern Ulsan fault (UF) using geo-electrical imaging: Implication for seismic hazard assessment in an urbanized area, *Journal of Geodynamics*, **151**, 101919.

Nguyen, F., Garambois, S., Chardon, D., Hermitte, D., Bellier, O., & Jongmans, D., 2007. Subsurface electrical imaging of anisotropic formations affected by a slow active reverse fault, Provence, France, *Journal of Applied Geophysics*, **62**(4), 338–353.

Nickschick, T., Flechsig, C., Mrlina, J., Oppermann, F., Löbig, F., & Günther, T., 2019. Large-scale electrical resistivity tomography in the Cheb Basin (Eger Rift) at an International Continental Drilling Program (ICDP) monitoring site to image fluid-related structures, *Solid Earth*, **10**(6), 1951–1969.

Olayinka, A. I. & Yaramanci, U., 2000. Use of block inversion in the 2-D interpretation of apparent resistivity data and its comparison with smooth inversion, *Journal of Applied Geophysics*, **45**(2), 63–81.

Orellana, L. F., Giorgetti, C., & Violay, M., 2019. Contrasting Mechanical and Hydraulic Properties of Wet and Dry Fault Zones in a Proposed Shale-Hosted Nuclear Waste Repository, *Geophysical Research Letters*, **46**(3), 1357–1366.

Reynolds, J. M., 2011. *An introduction to applied and environmental geophysics*, Jhon Wiley & Sons, Ltd, 2nd edn.

Röckel, L., Ahlers, S., Müller, B., Reiter, K., Heidbach, O., Henk, A., Hergert, T., & Schilling, F., 2022. The analysis of slip tendency of major tectonic faults in Germany, *Solid Earth*, **13**(6), 1087–1105.

Ronczka, M., Hellman, K., Günther, T., Wisén, R., & Dahlin, T., 2017. Electric resistivity and seismic refraction tomography: A challenging joint underwater survey at Äspö Hard Rock Laboratory, *Solid Earth*, **8**(3), 671–682.

Rønning, J. S., Ganerød, G. V., Dalsegg, E., & Reiser, F., 2014. Resistivity mapping as a tool for identification and characterisation of weakness zones in crystalline bedrock: definition and testing of an interpretational model, *Bulletin of Engineering Geology and the Environment*, **73**(4), 1225–1244.

Roques, C., Bour, O., Aquilina, L., Dewandel, B., Leray, S., Schroetter, J. M., Longuevergne, L., Le Borgne, T., Hochreutener, R., Labasque, T., Lavenant, N., Vergnaud-Ayraud, V., & Mougin, B., 2014. Hydrological behavior of a deep sub-vertical fault in crystalline basement and relationships with surrounding reservoirs, *Journal of Hydrology*, **509**, 42–54.

Rücker, C., Günther, T., & Wagner, F. M., 2017. pyGIMLi: An open-source library for modelling and inversion in geophysics, *Computers and Geosciences*, **109**, 106–123.

Sana, H., Taborik, P., Valenta, J., Bhat, F. A., Flašar, J., Štěpančíkova, P., & Khwaja, N. A., 2021. Detecting active faults in intramountain basins using electrical resistivity tomography: A focus on Kashmir Basin, NW Himalaya, *Journal of Applied Geophysics*, **192**.

Saribudak, M. & Hawkins, A., 2019. Hydrogeopysical characterization of the Haby Crossing fault, San Antonio, Texas, USA, *Journal of Applied Geophysics*, **162**, 164–173.

Schütze, C., Vienken, T., Werban, U., Dietrich, P., Finizola, A., & Leven, C., 2012. Joint application of geophysical methods and Direct Push-soil gas surveys for the improved delineation of buried fault zones, *Journal of Applied Geophysics*, **82**, 129–136.

Shewchuk, J. R., 1996. Triangle: Engineering a 2D quality mesh generator and Delaunay triangulator, in *Applied Computational Geometry Towards Geometric Engineering*, pp. 203–222, eds Lin, M. C. & Manocha, D., Springer.

Shipton, Z. K., Evans, J. P., Kirschner, D., Kolesar, P. T., Williams, A. P., & Heath, J., 2004. Analysis of CO ¡sub¿2¡/sub¿ leakage through 'low-permeability' faults from natural reservoirs in the Colorado Plateau, east-central Utah, *Geological Society, London, Special Publications*, **233**(1), 43–58.

Smith, E. & Carr, B., 2024. Defining Hydrogeophysical Layers With Multi-Scale Geophysics for Increased Understanding of Mountain Basin Recharge, *Journal of Geophysical Research: Solid Earth*, **129**(10).

Sproule, T. G., Spinelli, G. A., Wilson, J. L., Fort, M. D., Mozley, P. S., & Ciarico, J., 2021. The Effects of Fault-Zone Cementation on Groundwater Flow at the Field Scale, *Groundwater*, **59**(3), 396–409.

Tillner, E., Kempka, T., Nakaten, B., & Kühn, M., 2013. Brine migration through fault zones: 3D numerical simulations for a prospective CO2 storage site in Northeast Germany, *International Journal of Greenhouse Gas Control*, **19**, 689–703.

Torrese, P. & Pilla, G., 2021. 1D-4D electrical and electromagnetic methods revealing fault-controlled aquifer geometry and saline water uprising, *Journal of Hydrology*, **600**, 126568.

Tronicke, J., Paasche, H., & Böniger, U., 2011. Joint global inversion of GPR and P-wave seismic traveltimes using particle swarm optimization, in *6th International Workshop on Advanced Ground Penetrating Radar IEEE*, pp. 1–4, IEEE.

Tronicke, J., Paasche, H., & Böniger, U., 2012. Crosshole traveltime tomography using particle swarm optimization: A near-surface field example, *Geophysics*, **77**(1), R19–R32.

Tso, C.-H. M., Kuras, O., Wilkinson, P. B., Uhlemann, S., Chambers, J. E., Meldrum, P. I., Graham, J., Sherlock, E. F., & Binley, A., 2017. Improved characterisation and modelling of measurement errors in electrical resistivity tomography (ERT) surveys, *Journal of Applied Geophysics*, **146**, 103–119.

Tso, C. H. M., Iglesias, M., Wilkinson, P., Kuras, O., Chambers, J., & Binley, A., 2021. Efficient multiscale imaging of subsurface resistivity with uncertainty quantification using ensemble Kalman inversion, *Geophysical Journal International*, **225**(2), 887–905.

Vanneste, K., Verbeeck, K., & Petermans, T., 2008. Pseudo-3D imaging of a low-slip-rate, active normal fault using shallow geophysical methods: The Geleen fault in the Belgian Maas River valley, *Geophysics*, **73**(1), B1–B9.

Wagner, F. M. & Uhlemann, S., 2021. An overview of multimethod imaging approaches in environmental geophysics, in *Advances in Geophysics*, vol. 62, pp. 1–72, Academic Press Inc.

Wang, Z., Juhlin, C., Lü, Q., Ruan, X., Liu, Z., Yu, C., & Chen, M., 2025. High-resolution seismic reflection surveying to delineate shallow subsurface geological structures in the karst area of Shenzhen, China, *Solid Earth*, **16**(8), 761–773.

Watts, H., Booth, A. D., Clark, R. A., & Reinardy, B. T., 2023. The sensitivity of seismic refraction velocity models to survey geometry errors, assessed using Monte Carlo analysis, *Journal of Applied Geophysics*, **208**(November 2022), 104888.

Wellmann, J. F., Horowitz, F. G., Schill, E., & Regenauer-Lieb, K., 2010. Towards incorporating uncertainty of structural data in 3D geological inversion, *Tectonophysics*, **490**(3-4), 141–151.

Wheelock, B., Constable, S., & Key, K., 2015. The advantages of logarithmically scaled data for electromagnetic inversion, *Geophysical Journal International*, **201**(3), 1765–1780.

White, D. J., 1989. Two-Dimensional Seismic Refraction Tomography, *Geophysical Journal International*, **97**(2), 223–245.

Wunderlich, T., Fischer, P., Wilken, D., Hadler, H., Erkul, E., Mecking, R., Günther, T., Heinzelmann, M., Vött, A., & Rabbel, W., 2018. Constraining electric resistivity tomography by direct push electric conductivity logs and vibracores: An exemplary study of the Fiume Morto silted riverbed (Ostia Antica, western Italy), *Geophysics*, **83**(3), B87–B103.

Zarroca, M., Linares, R., Bach, J., Roqué, C., Moreno, V., Font, L., & Baixeras, C., 2012. Integrated geophysics and soil gas profiles as a tool to characterize active faults: The Amer fault example (Pyrenees, NE Spain), *Environmental Earth Sciences*, **67**(3), 889–910.

Zhang, Y., Borisov, D., Abbasi, S., Miller, R. D., & Sloan, S. D., 2025. Using transfer learning to enhance void detection and shear wave velocity model inversion from near-surface seismic shot gathers, *Journal of Applied Geophysics*, **240**, 105780.

Zhou, J., Revil, A., Karaoulis, M., Hale, D., Doetsch, J., & Cuttler, S., 2014. Image-guided inversion of electrical resistivity data, *Geophysical Journal International*, **197**(1), 292–309.